



Available online at www.sciencedirect.com

ScienceDirect

Comput. Methods Appl. Mech. Engrg. 416 (2023) 116391

**Computer methods
in applied
mechanics and
engineering**

www.elsevier.com/locate/cma

A hole-filling based approach to controlling structural complexity in topology optimization

Yunzhen He^a, Zi-Long Zhao^b, Xiaoshan Lin^a, Yi Min Xie^{a,*}

^a Centre for Innovative Structures and Materials, School of Engineering, RMIT University, Melbourne 3001, Australia
^b Institute of Solid Mechanics, School of Aeronautic Science and Engineering, Beihang University, Beijing 100191, China

Received 31 January 2023; received in revised form 3 August 2023; accepted 17 August 2023

Available online 10 September 2023

Abstract

Shape and topology optimization problems are usually associated with geometrical restrictions. Effective control of structural complexity during the optimization process is important for various considerations, e.g., functionality, manufacturability, and aesthetics. Most existing approaches characterize structural complexity as the number of cavities. However, for three-dimensional structures, the genus (i.e., the number of tunnels) should also be considered as an additional topological constraint. In this paper, a hole-filling method is integrated into the bi-directional evolutionary structural optimization (BESO) computational framework to control the number and size of existing cavities and tunnels during the form-finding process. In the hole-filling method, excess cavities are filled with solid material and excess tunnels are covered by building sheet-like patches. The minimum size of the truss-like components and the minimum thickness of the sheet-like components can be controlled separately. Several two- and three-dimensional compliance minimization problems are presented to demonstrate the effectiveness and potential applications of the proposed approach. The structural performances of the optimized structures with and without complexity control are compared and analyzed. The results show that the developed methodology can produce structurally efficient designs with controllable topologies. It is also demonstrated that the generation of sheet-like components can considerably increase the stiffness of the optimized structure. The proposed approach is capable of generating diverse and competitive designs for architects and engineers to achieve a fine balance between architectural novelty and structural efficiency.

© 2023 The Author(s). Published by Elsevier B.V. This is an open access article under the CC BY-NC-ND license (<http://creativecommons.org/licenses/by-nc-nd/4.0/>).

Keywords: Topology optimization; Structural complexity control; Diverse and competitive structural designs; Topological constraints

1. Introduction

Topology optimization methods have been widely used to find efficient structural layouts by spatially optimizing the material distribution within a prescribed design domain. In recent years, several optimization methods, e.g., the homogenization method [1,2], the solid isotropic material with penalization (SIMP) method [2,3], the bi-directional evolutionary structural optimization (BESO) method [4–7], and the level-set method [8,9] have undergone tremendous development. These methods have been successfully extended to a wide range of engineering applications, including advanced manufacturing [10–16], architectural design [17–24], biomechanical morphogenesis [25–29], civil engineering [30–35], and metamaterials [36,37].

* Corresponding author.

E-mail address: mike.xie@rmit.edu.au (Y.M. Xie).

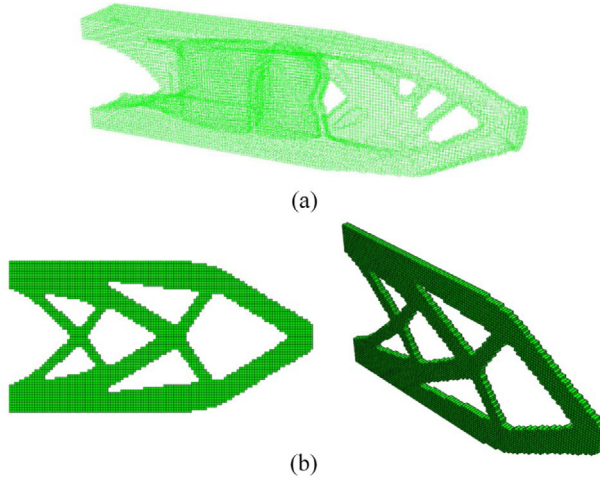


Fig. 1. (a) A three-dimensional structure with two cavities and four tunnels. (b) A two-dimensional structure with six cavities and its corresponding three-dimensional counterpart with six tunnels.

Although remarkable progress has been made in topology optimization, it remains a challenging issue to directly control the structural complexity in three-dimensional optimization problems. Structural complexity control (SCC) is important in practical applications because the optimized design often needs to satisfy different requirements. From a manufacturing point of view, SCC can be used to avoid complex structural geometries to ensure the optimized results are easy to fabricate [16,38]. For fail-safe structures, the use of SCC can improve structural redundancy to resist local failure [39–41]. In architectural design, void spaces (e.g., cavities and tunnels) may need to be reserved for both functional and aesthetic considerations [18,42].

The structural complexity of a three-dimensional continuum structure is closely related to the distribution and geometry of cavities and tunnels [43–45] (see Fig. 1a). Cavities are enclosed voids, easily identified using connected components search algorithms [46,47]. On the other hand, tunnels are essentially pathways running through the structure, and they can intersect with each other, making them less well-defined subsets of void elements. Consequently, identifying them separately can be challenging.

Unlike three-dimensional structures, characterizing structural topology in two-dimensional structures only requires the consideration of either cavities or tunnels, as they are equivalent topological features. This equivalence arises when a two-dimensional structure is treated as a single layer of a three-dimensional structure, transforming “two-dimensional” cavities into “three-dimensional” tunnels (see Fig. 1b). Hence, some existing SCC methods [48–52] employ the term “holes” (also referred to as tunnels in digital topology) to describe the two-dimensional structural topology. However, when extending these methods to three-dimensional SCC, their ability to control structural complexity falls short, as they can only control cavities, not tunnels. In this paper, we characterize the topology of two-dimensional structures by solely referring to their number of cavities.

The existing SCC approaches can be categorized into implicit and explicit methods. Using the implicit method, designers control the structural complexity without specifying the topological constraints. For example, filter techniques are commonly used to control the minimum length scale of structural members and eliminate the checkerboard pattern during the optimization process [53–55]. In recent years, several approaches have been developed to impose minimum or maximum length-scale constraints, e.g., the Heaviside projection-based method [56,57] and the structural skeleton-based method [58–60]. These approaches can change the structural details by imposing different length scale constraints. In addition to controlling the length scale, Kim et al. [61] developed an intelligent cavity creation method to indirectly control the number of cavities using the evolutionary structural optimization method. Besides, Clausen et al. [42] proposed a penalization method to introduce flexible void areas into the compliance minimization problem.

Using the explicit method, designers can directly constrain the number of cavities or tunnels. A moving morphable component based SCC method was proposed by constraining the number of effective structural components [62]. By integrating the concept of the structural skeleton into the level-set method, the number and size

Table 1

Comparative analysis of explicit SCC methods.

Explicit method	Number control (cavities)	Size control (cavities)	Number control (tunnels)	Size control (tunnels)
Moving morphable component method [62]	Yes	–	–	–
Level-set method [48]	Yes	Yes	–	–
Graph and set theory method [49]	Yes	Yes	–	–
2D Hole-Filling Method [50]	Yes	Yes	–	–
SIMP-based SCC [51]	Yes	–	–	–
Discrete variable-based method [52]	Yes	Yes	–	–
Quotient set design variable [68]	–	–	Yes	–
Topology-preserving method [20]	Yes	–	Yes	–

of cavities can be directly controlled by monitoring a series of level set functions [48]. Based on the graph theory and set theory, Zhao et al. [49] developed an explicit method which is capable of controlling the structural complexity directly in the optimization process. Under the BESO computational framework, Han et al. [50] developed a two-dimensional hole-filling method to control the maximum number of cavities in topology optimization. By adjusting the filter radius, Wang et al. [51] proposed a SIMP-based SCC approach to impose inequality constraints on the number of cavities. More recently, Liang et al. [52] used the Euler–Poincaré formula and the fluid flooding strategy to measure the number of cavities. In their methods, the number of cavities was controlled by the discrete variable topology optimization formulation which was solved by using the sequential approximate integer programming framework and the canonical relaxation algorithm.

The above SCC approaches can effectively control the number and/or size of cavities. It remains a challenging issue to control the number and size of tunnels for three-dimensional topology optimization. Different from the two-dimensional cases, cavities are rare features in three-dimensional optimization. Due to the length-scale constraint, the optimized three-dimensional structures are usually truss-like (i.e., open-walled structures with multiple tunnels) [63]. Moreover, cavities should be avoided in some cases for ease of fabrication [10,64,65]. For example, it is important to generate tunnels to eliminate enclosed cavities for additive manufacturing techniques such as selective laser sintering [66] and fused deposition modeling [67], as the unmelted powder or support structures need to be removed from the printed model.

In terms of realizing the genus (i.e., the number of tunnels) constraint for three-dimensional problems, Han et al. [68] proposed a quotient set design variable method based on the discrete variable topology optimization method. The quotient set design variable method is used to adjust the design variable update process to control the maximum genus. However, this method could not impose the equality constraint on the genus, so a precise SCC could not be guaranteed. More recently, a topology-preserving SCC method was proposed under the BESO computational framework to simultaneously constrain the number of tunnels and cavities by preserving the topological properties of the prescribed initial design [20]. In this work, tunnels and cavities need to be initially distributed, but the size of the tunnels cannot be controlled.

Most of the explicit SCC methods listed in Table 1 can control the number of cavities, with some also offering size adjustments. However, they notably fall short when it comes to generating SCC in three-dimensional structures. In particular, none of these methods provide a holistic solution for controlling both the number and size of tunnels, which is of great significance in three-dimensional topology optimization.

Inspired by the hole-closing algorithm for three-dimensional volumetric images [69,70], in this study, a hole-filling method is proposed and integrated into the BESO-based computational framework to constrain the number and size of cavities and tunnels for both two- and three-dimensional structures. In the hole-filling method, topological

constraints are imposed by filling in cavities and building patches to cover tunnels. The effectiveness and practical applicability of the developed approach are verified by several compliance minimization problems. The results show that the stiffness of the optimized design can be improved by limiting the number of tunnels. Thus, it further confirms that the stiffest design is not truss-like with multiple tunnels but sheet-like with many closed-walled shells [63].

The rest of the paper is organized as follows. Section 2 describes the BESO computational framework and the related topological constraints. Section 3 introduces basic notions for digital topology and the details of the hole-filling method, followed by the implementation details of the SCC approach. Section 4 presents several numerical examples to demonstrate the effectiveness of the SCC approach. Potential applications of the developed approach are illustrated by two examples in Section 5. In Section 6, the main conclusions from this study are summarized.

2. Topology optimization formulation

The SCC approach is developed based on the BESO method, which has been increasingly employed in a wide range of structural design problems [71]. In this section, the compliance minimization problems are considered as an example to realize SCC.

The optimization formulation for minimizing the structural compliance can be described in the frame of the finite element method as

$$\underset{\mathbf{X}}{\text{Minimize}} : C(\mathbf{X}) = \frac{1}{2} \mathbf{U}^T \mathbf{K} \mathbf{U} = \frac{1}{2} \sum_{i=1}^N x_i^p \mathbf{u}_i^T \mathbf{k}_i \mathbf{u}_i \quad (1)$$

$$\begin{aligned} \text{Subject to: } & V^* - \sum_{i=1}^n x_i v_i = 0 \\ & \tilde{g} \leq \tilde{G} \text{ and } S_k^{\tilde{G}} \geq S_*^{\tilde{G}} \\ & \tilde{c} \leq \tilde{C} \text{ and } S_j^{\tilde{C}} \geq S_*^{\tilde{C}} \end{aligned} \quad (2a)$$

$$\begin{aligned} \text{Subject to: } & V^* - \sum_{i=1}^n x_i v_i = 0 \\ & \tilde{g} = \tilde{G} \text{ and } S_k^{\tilde{G}} \geq S_*^{\tilde{G}} \\ & \tilde{c} = \tilde{C} \text{ and } S_j^{\tilde{C}} \geq S_*^{\tilde{C}} \end{aligned} \quad (2b)$$

where C is the mean structural compliance. $\mathbf{X} = \{x_i | i = 1, 2, \dots, N\}$ is the vector of elemental densities. x_i is the i th design variable with binary values of either 1 for solid elements or x_{\min} (0.001 in this paper) for void elements. N is the total number of elements. \mathbf{U} and \mathbf{K} are the global displacement vector and stiffness matrix, respectively. p is the penalty exponent [3], which is set as 3 in this paper. \mathbf{u}_i is the elemental displacement vector and \mathbf{k}_i is the stiffness matrix of element i . $V^* = V \times v_f$ is the target volume of the final structure. V is the total volume of the design domain and v_f is the target volume fraction of material. v_i is the volume of an individual element i . \tilde{g} and \tilde{c} are the current numbers of tunnels and cavities during the optimization process, respectively. \tilde{G} and \tilde{C} are the target numbers of holes and cavities in the final structure, respectively. $S_k^{\tilde{G}}$ and $S_j^{\tilde{C}}$ are the sizes (volumes) of the k th tunnel and j th cavity, respectively. $S_*^{\tilde{G}}$ and $S_*^{\tilde{C}}$ are the prescribed minimum sizes of the tunnels and cavities, respectively.

According to the initial design, the problem of controlling cavities and tunnels can be divided into the following two cases: (1) the number of initial cavities or tunnels is less than the target number [see Eq. (2a)]; and (2) the number of initial cavities or tunnels is equal to or greater than the target number [see Eq. (2b)]. The calculation method for the number of cavities and tunnels and the implementation of the hole-filling method will be discussed in the following sections.

The design variables are updated iteratively according to the relative ranking of the sensitivities. By using the adjoint method [7], the gradient of the objective function C with regard to the design variable x_i can be calculated as

$$\frac{\partial C}{\partial x_i} = -\frac{1}{2} p x_i^{p-1} \mathbf{u}_i^T \mathbf{k}_i \mathbf{u}_i \quad (3)$$

The sensitivity of element i is defined as

$$\alpha_i = -\frac{1}{pv_i} \frac{\partial C}{\partial x_i} \quad (4)$$

To avoid checkerboard pattern and mesh-dependency issues, the following filtering scheme is adopted to process the raw sensitivity [72].

$$\tilde{\alpha}_i = \frac{\sum_{j=1}^N w_{ij} \alpha_j}{\sum_{j=1}^N w_{ij}} \quad (5)$$

$$w_{ij} = \max(0, r_f - d_{ij}) \quad (6)$$

where w_{ij} is the weight function, r_f the filter radius, and d_{ij} the distance between the centers of elements i and j .

In order to stabilize the optimization process and achieve convergent solutions, the smoothed sensitivity of the current iteration is modified by using its historical information as follows [6].

$$\bar{\alpha}_i = \frac{\tilde{\alpha}_i^{(n)} + \tilde{\alpha}_i^{(n-1)}}{2}, (n \geq 2) \quad (7)$$

where $\tilde{\alpha}_i^{(n)}$ and $\tilde{\alpha}_i^{(n-1)}$ are the smoothed sensitivities of element i in the n th and $(n-1)$ th iterations, respectively. The element update scheme is based on the relative ranking of the averaged sensitivities and the target volume. The target volume $V^{(n)}$ of material in the n th iteration is

$$V^{(n)} = \max \{V^*, V^{(n-1)}(1 - \delta)\} \quad (8)$$

where the evolutionary ratio δ is set as 0.02 in this study.

The solid elements with sensitivities lower than a threshold are removed from the design domain, and the removed elements with sensitivities higher than the threshold are readmitted to the design domain. In this paper, the sensitivity threshold is determined by the bisection method [73].

The optimization process terminates as the material volume decreases to the target value V^* and the following convergence criterion is satisfied [7]:

$$\frac{\left| \sum_{i=1}^Z C_{n-i+1} - \sum_{i=1}^Z C_{n-Z-i+1} \right|}{\sum_{i=1}^Z C_{n-i+1}} \leq \tau \quad (9)$$

where n is the current iteration number. τ is the tolerance which is set as 0.001 in this paper. Z is set to be 5, which implies that the change in the mean compliance over the previous 10 iterations is acceptably small.

3. Structural complexity control

In the SCC approach, the topological constraints are imposed by using the hole-filling method. The hole-filling method is a modified version of the hole-closing algorithm proposed by Aktouf et al. [69,70]. The original hole-closing algorithm aims to suppress tunnels and cavities in a structure by building solid closures. However, it cannot identify each closure separately. Thus, the number of distinct closures in the structure is unknown, and it is not possible to impose SCC precisely. In this section, a hole-filling method is integrated into the BESO method to explicitly constrain the number of tunnels and cavities of the structure.

Under the BESO-based computational framework, the solid-void optimized design corresponds to a binary image consisting of solid and void voxels. Therefore, in the following description, voxel and element are interchangeable concepts. The hole-filling method developed in this study is guided by the concept of digital topology. In Section 3.1, the relevant aspects of digital topology are introduced. A more extensive review is provided in [74]. In Section 3.2, the hole-filling method is presented. Section 3.3 describes the implementation of the proposed hole-filling method. Section 3.4 presents the technique to implement the minimum length scale control of the structure. In Section 3.5, the numerical implementation procedure of the SCC approach is summarized.

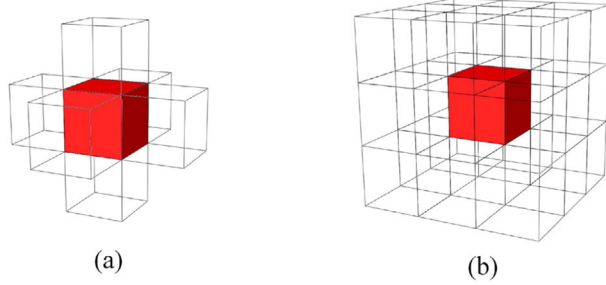


Fig. 2. Definition of neighborhood. The transparent voxels in (a) and (b) are respectively the 6-neighbors $N_6^*(\tilde{v})$ and 26-neighbors $N_{26}^*(\tilde{v})$ of the red voxel \tilde{v} at the center.

3.1. Basic topological notions

3.1.1. Neighborhood and connectivity

In this paper, \mathbb{Z} denotes the set of integers, and we denote $E = \mathbb{Z}^3$. A voxel $\tilde{v} \in E$ is defined by $(\tilde{x}_1, \tilde{x}_2, \tilde{x}_3)$ with $\tilde{x}_i \in \mathbb{Z}$. The set of $N_n(\tilde{v})$ is called the n -neighborhood of the voxel \tilde{v} . We consider the following two types of neighborship:

$$N_6(\tilde{v}) = \{\tilde{v}' \in E \mid |\tilde{x}_1 - \tilde{x}'_1| + |\tilde{x}_2 - \tilde{x}'_2| + |\tilde{x}_3 - \tilde{x}'_3| \leq 1\} \quad (10)$$

$$N_{26}(\tilde{v}) = \{\tilde{v}' \in E \mid \max(|\tilde{x}_1 - \tilde{x}'_1|, |\tilde{x}_2 - \tilde{x}'_2|, |\tilde{x}_3 - \tilde{x}'_3|) \leq 1\} \quad (11)$$

As shown in Fig. 2, we define $N_n^*(\tilde{v}) = N_n(\tilde{v}) \setminus \{\tilde{v}\}$ ($n = 6, 26$). Any individual voxel v' in $N_n^*(\tilde{v})$ is n -adjacent to v , or in other words, v' is an n -neighbor of v . An n -path π is a sequence of voxels $\tilde{v}_0, \dots, \tilde{v}_i, \dots, \tilde{v}_k$, with \tilde{v}_i n -adjacent to \tilde{v}_{i-1} . The set of all voxels in the design domain $\tilde{v} \in \tilde{V} = \tilde{V}_s \cup \tilde{V}_e$ is composed of the solid voxels \tilde{V}_s and the void voxels \tilde{V}_e , which yield two corresponding mesh objects referred to as $M_s = M(\tilde{V}_s)$ and $M_e = M(\tilde{V}_e)$, respectively.

An object $M_s \subseteq E$ is n -connected, if there is an n -path between any two voxels of M_s . The set composed of all the n -connected components of M_s is denoted as $\hat{C}_n(M_s)$. Moreover, to avoid connectivity paradoxes [74], it is important to use different definitions of neighborship for solid and void objects, respectively. For example, if we use the n -connectivity for the solid object M_s , then we need to use another m -connectivity for the corresponding void object M_e . In this paper, we have $(n, m) = (26, 6)$.

3.1.2. Topological numbers

Before introducing the topological numbers, several definitions [75] are first reviewed, which allow us to extract the topological characteristics of a voxel.

Let $M_s \subseteq E$ and $\tilde{v} \in E$. The geodesic n -neighborhood of \tilde{v} inside $M_s \subseteq E$ of order k is $N_n^k(\tilde{v}, M_s)$ and is defined recursively as follows:

$$N_n^1(\tilde{v}, M_s) = N_n^*(\tilde{v}) \cap M_s \quad (12)$$

$$\text{and } N_n^k(\tilde{v}, M_s) = \cup \{N_n(\tilde{v}') \cap N_{26}^*(\tilde{v}) \cap M_s, \tilde{v}' \in N_n^{k-1}(\tilde{v}, M_s)\} \quad (13)$$

As shown in Fig. 3, $N_n^k(\tilde{v}, M_s)$ is the set composed of all voxels \tilde{v}' of $N_{26}^*(\tilde{v}) \cap M_s$ such that there is an n -path π from \tilde{v} to \tilde{v}' of length less than or equal to k . All points of π , except \tilde{v} , is included in $N_{26}^*(\tilde{v}) \cap M_s$.

The geodesic neighborhoods $G_n(\tilde{v}, M_s)$ are defined as

$$G_6(\tilde{v}, M_s) = N_6^2(\tilde{v}, M_s), G_{26}(\tilde{v}, M_s) = N_{26}^1(\tilde{v}, M_s) \quad (14)$$

Then the topological numbers of a voxel \tilde{v} are defined as [75]

$$T_n(\tilde{v}, M_s) = |\hat{C}_n[G_n(\tilde{v}, M_s)]| \quad (15)$$

$$\overline{T}_m(\tilde{v}, M_e) = |\hat{C}_m[G_m(\tilde{v}, M_e)]| \quad (16)$$

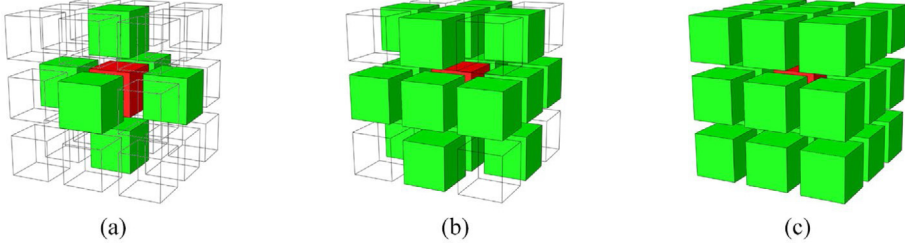


Fig. 3. Geodesic neighborhoods of a voxel \tilde{v} . Green voxels represent (a) $N_6^1(\tilde{v}, M_s)$, (b) $N_6^2(\tilde{v}, M_s)$, and (c) $N_6^3(\tilde{v}, M_s)$, where $N_{26}(\tilde{v}) \subset M_s$. For all $k \geq 3$, $N_6^k(\tilde{v}, M_s) = N_{26}^*(\tilde{v})$. (For interpretation of the references to color in this figure legend, the reader is referred to the web version of this article.)

Table 2
Topological classification of a voxel.

Type A	Isolated point	$T_n(\tilde{v}, M_s) = 0$	—
Type B	Interior point	—	$\overline{T}_m(\tilde{v}, M_e) = 0$
Type C	Border point	—	$\overline{T}_m(\tilde{v}, M_e) \neq 0$
Type D	Simple point	$T_n(\tilde{v}, M_s) = 1$	$\overline{T}_m(\tilde{v}, M_e) = 1$
Type E	1D isthmus	$T_n(\tilde{v}, M_s) \geq 2$	—
Type F	2D isthmus	—	$\overline{T}_m(\tilde{v}, M_e) \geq 2$

where $|\hat{C}_n(M_s)|$ denotes the number of the n -connected components of M_s (i.e., the cardinality of M_s). The topological characteristic of a voxel can be described by the above two numbers. According to the values of $T_n(\tilde{v}, M_s)$ and $\overline{T}_m(\tilde{v}, M_e)$, a voxel \tilde{v} can be classified into a certain topological type [76] (see Table 2). As shown in Fig. 4, the topological classification of a voxel \tilde{v} can be locally defined by the number of connected components in $N_{26}(\tilde{v})$. In digital topology, the topological numbers can be used to describe the local topological configuration of a voxel. For example, the concept of simple points is essential for topology-preserving transformations in discrete spaces, e.g., the thinning or skeletonization algorithms [77,78]. Specifically, a voxel is regarded as a simple point if its removal does not change the structural topology (Fig. 4b). A voxel is called a two-dimensional isthmus if its removal connects void regions of the structure (Fig. 4c). Similarly, if deletion of a voxel locally disconnects the structure, we call this voxel a one-dimensional isthmus (Fig. 4d).

3.2. Hole-filling method

The hole-filling method is developed here based on the hole-closing algorithm [69,70]. The pseudocode of the hole-closing algorithm is presented in Table 3. The hole-closing algorithm starts from a bounding box M_B that contains the input solid structure M_s and has no holes or tunnels (see line 1 in Table 3 and Fig. 5b). The algorithm proceeds by iteratively removing solid border voxels of $M_B \setminus M_s$ which are not 2D isthmus (line 7). The set difference $M_B \setminus M_s$ is defined by $M_B \setminus M_s = \{\tilde{v} | \tilde{v} \in M_B \text{ and } \tilde{v} \notin M_s\}$. Solid voxels with at least one void voxel in their $N_6^*(\tilde{v})$ are defined as solid border voxels (line 7). The voxel removal process is ordered by computing the distance from each solid border voxel \tilde{v} to the input structure M_s , which denotes by:

$$d(\tilde{v}, M_s) = \min \{d(\tilde{v}, \tilde{v}'); \tilde{v}' \in M_s\} \quad (17)$$

where d is the distance in E . The border voxels are ranked and processed according to their distance from M_s in descending order. In this paper, we use the distance transform algorithm [79] to calculate these distances. The distance transform algorithm can turn a binary mesh model with featured voxels and non-featured voxels into another digital image in which the value of each non-featured voxel is its distance to the nearest featured voxels (Fig. 6). In discrete spaces, the distance between voxels can be calculated by several distance metrics, including the city block (denoted as d_6), chessboard (denoted as d_{26}), and Euclidean distance (denoted as d_E) metrics. For example, the city block and chessboard distances are calculated by the lengths of the shortest 6-path and 26-path between two voxels, respectively. The hole-closing task terminates when all the remaining voxels of $M_B \setminus M_s$ are non-removable (line 4).

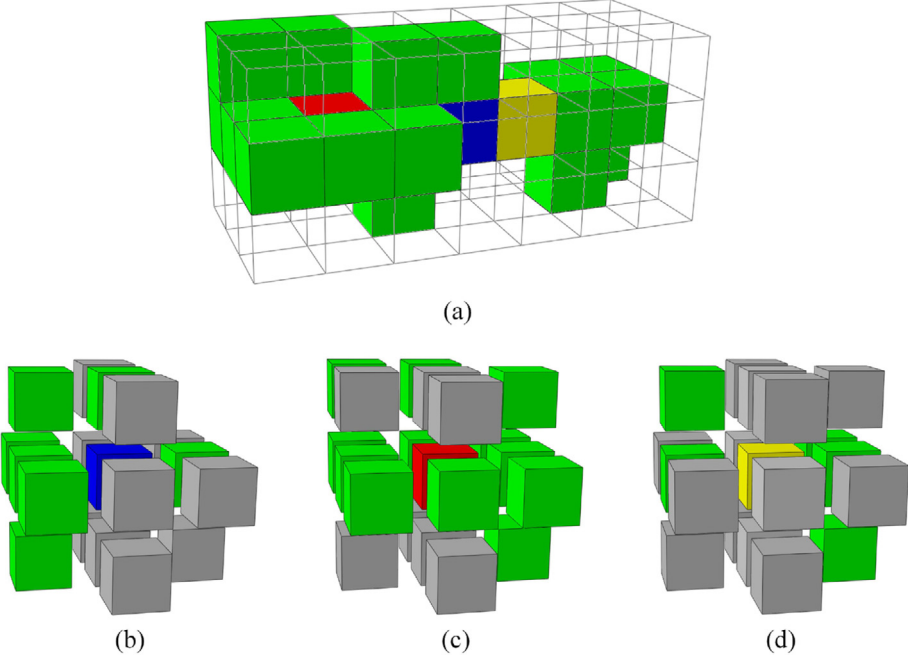


Fig. 4. Illustration of a simple point (blue voxel), a two-dimensional isthmus (red voxel) and a one-dimensional isthmus (yellow voxel) in a voxel complex M_s . The (26, 6) connectivity is assumed. (a) The voxel complex M_s . (b) An example of a simple point. The one connected component of $G_{26}(\tilde{v}, M_s)$ is presented in green, while one connected component of $G_6(\tilde{v}, M_e)$ is presented in gray [$T_{26}(\tilde{v}, M_s) = 1$, $\bar{T}_6(\tilde{v}, M_e) = 1$]. (c) An example of a 2D isthmus. The one connected component of $G_{26}(\tilde{v}, M_s)$ is presented in green, while two connected components of $G_6(\tilde{v}, M_e)$ are presented in gray [$T_{26}(\tilde{v}, M_s) = 1$, $\bar{T}_6(\tilde{v}, M_e) = 2$]. (d) An example of a 1D isthmus. Two connected components of $G_{26}(\tilde{v}, M_s)$ are presented in green, while one connected component of $G_6(\tilde{v}, M_e)$ is presented in gray [$T_{26}(\tilde{v}, M_s) = 2$, $\bar{T}_6(\tilde{v}, M_e) = 1$]. (For interpretation of the references to color in this figure legend, the reader is referred to the web version of this article.)

Table 3
Hole-closing algorithm.

Input: The solid structure M_s	
1	Generating a bounding box $M_B = M_s \cup M_e$ # all voxels in M_B are initially set as solid
2	$N_{\text{non}} = 0$ # auxiliary counter for the non-removable voxels
3	$N_{\text{remain}} =$ The number of voxels in $M_B \setminus M_s$
4	While $N_{\text{remain}} \neq N_{\text{non}}$ do
5	$N_{\text{non}} = 0$
6	for $\tilde{v} \in M_B$ do
7	if $\left\{ \begin{array}{l} \tilde{v} \in M_B \setminus M_s \text{ and} \\ \text{any } \tilde{v}' \text{ in } N_6(\tilde{v}) \text{ is void and} \\ \tilde{v} \text{ is at the greatest distance from } M_s \text{ and} \\ \tilde{v} \text{ is not 2D isthmus} \end{array} \right\}$
8	$M_B \leftarrow M_B \setminus \tilde{v}$ # the removed solid voxel is reclassified as void
9	break
10	else
11	$N_{\text{non}} = N_{\text{non}} + 1$ # count the non-removable voxels
12	end
13	$N_{\text{remain}} =$ The number of voxels in $M_B \setminus M_s$
14	end
Output: The updated bounding box M_B	

In the final result, for each remaining voxel \tilde{v} of $M_B \setminus M_s$, the structure $M_B \setminus \tilde{v}$ has a tunnel or a cavity. The final structure is referred to as the topological hull of M_s [69,70] which is denoted as $\Theta(M_s)$ in this paper. As shown

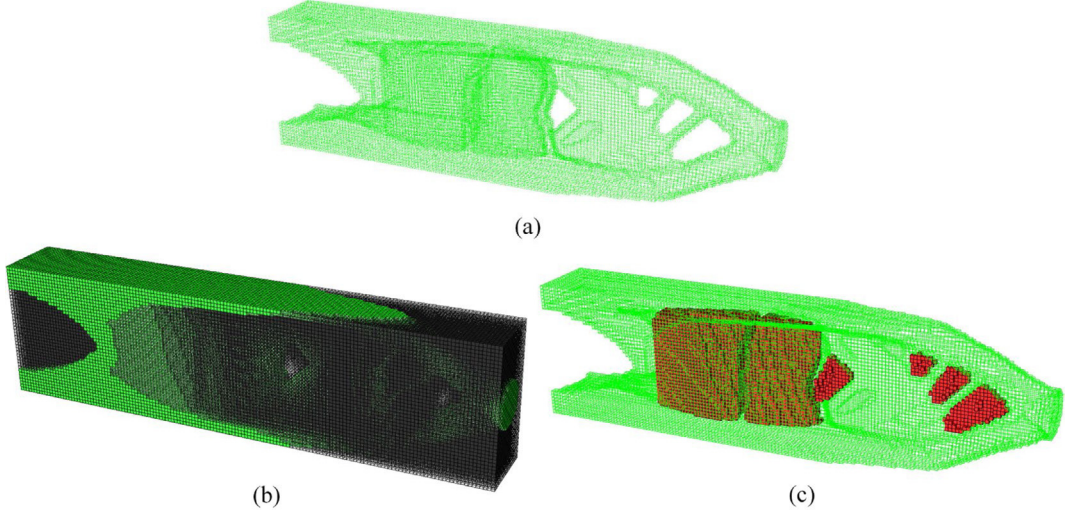


Fig. 5. Application of hole closing algorithm to a 3D structure. (a) Initial structure M_s with two cavities and four tunnels. (b) Bounding box M_B consisting of the structure M_s and the light-shaded voxels M_e . (c) Obtained structure with all cavities and tunnels closed (the red voxels are the remaining voxels of the set M_e). (For interpretation of the references to color in this figure legend, the reader is referred to the web version of this article.)

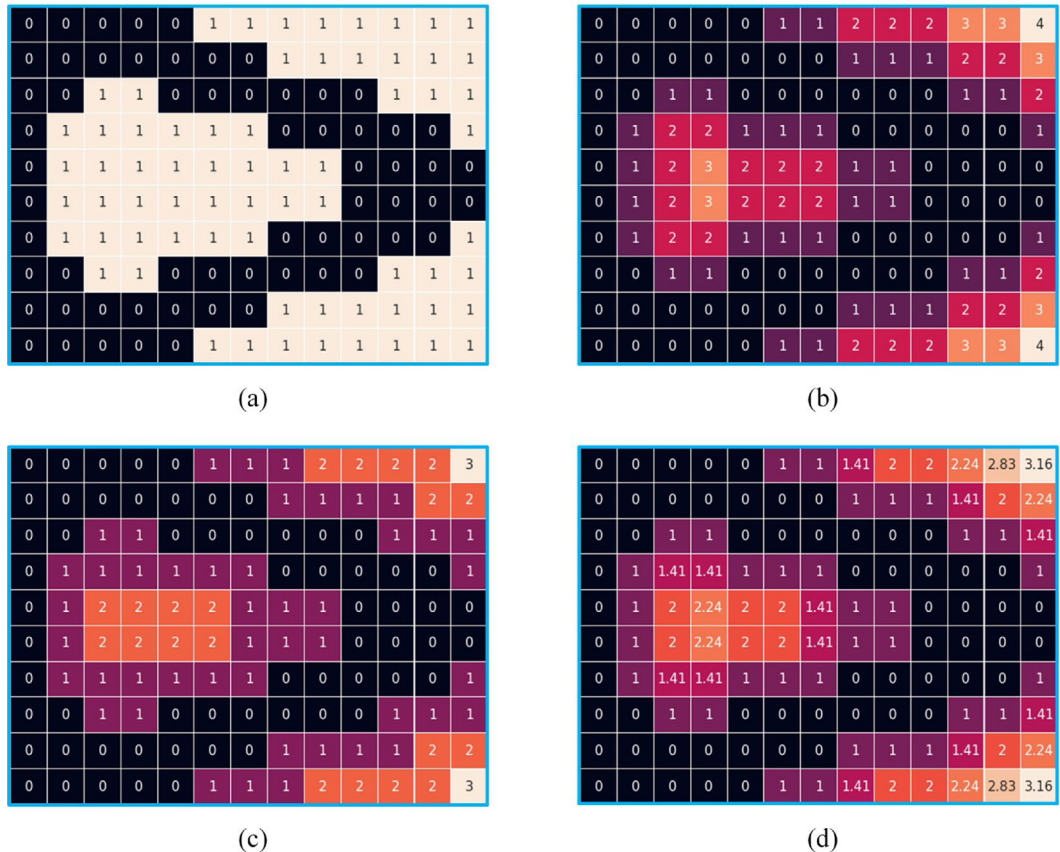


Fig. 6. Illustration of distance transformation. (a) A binary model with featured (black voxels) and non-featured voxels (white voxels). (b), (c), and (d) are the resulting images according to the city block, chessboard, and Euclidean distance metrics, respectively. (For interpretation of the references to color in this figure legend, the reader is referred to the web version of this article.)

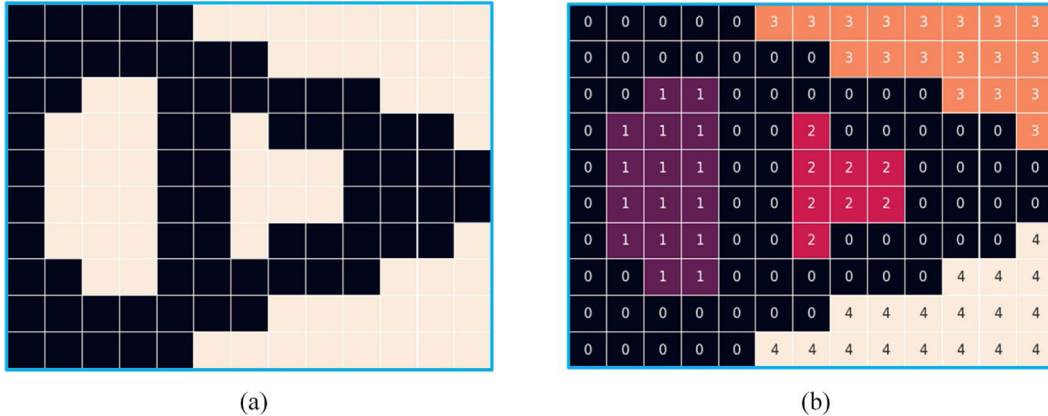


Fig. 7. Illustration of connected-component labeling. (a) An original binary model with featured (white voxels) and non-featured voxels (black voxels). (b) Resulting image after component labeling of featured. (For interpretation of the references to color in this figure legend, the reader is referred to the web version of this article.)

in Fig. 5c, the remaining voxels of $M_B \setminus M_s$ not only close all cavities of M_s , but also cover all tunnels of M_s by building one-voxel-thick solid patches.

It should be noted that the geometry of the obtained topological hull depends on the sequencing of voxel removal [69,70]. Thus, a given structure will have several different topological hulls based on different distance metrics. In this paper, we use the Euclidean distance d_E as a constraint to restrict the choice of potential points to build the topological hull (Fig. 6d).

By using the hole-closing algorithm, the input structure M_s is replaced by a topological hull $\Theta(M_s)$ with closures closing all cavities and tunnels. To precisely control the number of cavities and tunnels, the first issue to be solved is to identify these closures separately. In this study, the hole-closing algorithm, the connected-component labeling (CCL) algorithm [46,47], and the set theory are combined to investigate the number of distinct closures for cavities and tunnels in a structure.

The CCL algorithm is a basic algorithm dealing with object detection. It collects featured voxels from the same connected component, and subsets of connected components are labeled uniquely (Fig. 7). The identification of cavities can be easily realized by using the CCL algorithm and the set theory. The void voxels can be divided into two different groups, including the enclosed voids (cavities) Ω_C , and the non-enclosed voids $\Omega_{\bar{C}}$. By using the CCL algorithm, the void voxels that belong to different regions are categorized into different sets and denoted as $\tilde{\Omega}_e$ ($e = 1, 2, \dots, n$). $\tilde{\Omega}_e$ belongs to Ω_C if

$$\tilde{\Omega}_e \cap \partial\Omega = \emptyset, \quad (18)$$

where $\partial\Omega$ denotes the set of voxels that are located at the edge of the design domain. Otherwise, it belongs to $\Omega_{\bar{C}}$. Fig. 8 illustrates the identification of cavities by using Eq. (18). Then, we put each set $\tilde{\Omega}_e \in \Omega_C$ into a new set Ω_C^* , and Ω_C^* is ordered based on the cardinality of each subset $\tilde{\Omega}_e \in \Omega_C$ in ascending order. Finally, the number of cavities in the structure, denoted as \tilde{c} , can be calculated by the cardinality of $\Omega_C^* = \{\tilde{\Omega}_1, \tilde{\Omega}_2, \dots, \tilde{\Omega}_{\tilde{c}}\}$.

Unlike the cavities, which are well-delimited sub-regions, the closures for different tunnels may merge together (see Fig. 9a and b). Therefore, it is not possible to directly use the CCL algorithm to identify the closure for each tunnel. To solve this problem, a simple strategy consisting of three steps is proposed to precisely segment these closures.

In the first step, the closures of structural tunnels Ω_T are obtained by computing the set difference between $\Theta(M_s)$ and $M_s \cup \Omega_C$ (see red voxels in Fig. 9a and b). Then, the regional maxima of the distance transform value $d(\tilde{v}, M_s)$ of each voxel $\tilde{v} \in \Omega_T$ is obtained as tunnel identifiers. A regional maximum M_{\max} of a binary image is a connected component of voxels with value t whose neighboring voxels have a value strictly smaller than t [80]

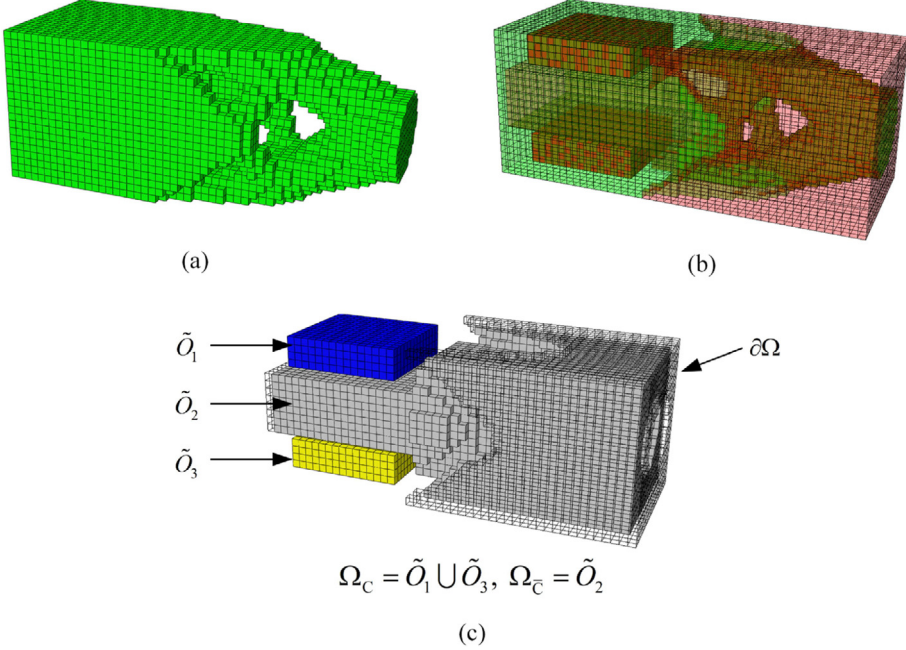


Fig. 8. Identification of cavities in the design domain. (a) Solid structure. (b) Perspective view of both solid (green) and void (red) voxels. (c) Void voxels of different sets are highlighted in different colors. The shaded voxels in set \tilde{O}_2 are the intersected voxel with set $\partial\Omega$. (For interpretation of the references to color in this figure legend, the reader is referred to the web version of this article.)

(see Fig. 9c and d), i.e., M_{\max} is a regional maximum if and only if M_{\max} is connected and

$$\begin{cases} \forall \tilde{v} \in M_{\max}, & d(\tilde{v}, M_s) = t \\ \forall \tilde{v} \in \delta(M_{\max}) \setminus M_{\max}, & d(\tilde{v}, M_s) \leq t \end{cases}, \quad (19)$$

where $\delta(M_{\max})$ denotes the connected set of voxels of M_{\max} and the direct 26-connected voxels whose distance from any $\tilde{v} \in M_{\max}$ is equal to 1. As shown in Fig. 9c and d, the distance transform value of each tunnel closure will have at least one regional maximum. Therefore, the number of regional maxima in Ω_T can be used to approximately measure the number of tunnel closures in a topological hull $\Theta(M_s)$.

In the second step, all regional maxima are distinguished and labeled by using the CCL algorithm. The e th regional maximum is denoted as M_{\max}^e ($e = 1, 2, \dots, m$). Then, we iteratively remove voxels of $\Theta(M_s) \setminus M_{\max}^e \setminus M_s$ which are not 2D isthmus until no voxels are removable (see Fig. 9e and f). The final structure, denoted as $\tilde{\Theta}(M_s)_e$, is a topological hull of M_s with one opening tunnel. The voxel removal is iteratively performed based on each regional maximum to obtain the corresponding $\tilde{\Theta}(M_s)_e$, where the iteration variable e increases from 1 to m . An individual tunnel closure (denoted as \tilde{T}_e) can be obtained by computing the set difference between $\Theta(M_s)$ and $\tilde{\Theta}(M_s)_e$.

Each tunnel closure will have at least one regional maximum, and the number of regional maxima may exceed the number of distinct closures, so overcounting of closures is likely to happen. As shown in Fig. 10, if this structure is treated as a three-dimensional structure with one layer of elements, two regional maxima are identified using Eq. (19). Although there is only one tunnel in Fig. 10a, by using the above technique, two identical voxel sets are created. Thus, in the third step, duplicate sets of \tilde{T}_e ($e = 1, 2, \dots, m$) are removed and the remaining sets are put into a new set Ω_T^* which is ordered by the cardinality of each subset \tilde{T}_e in ascending order. The number of tunnels, denoted as \tilde{g} , can be calculated by the cardinality of $\Omega_T^* = \{\tilde{T}_1, \tilde{T}_2, \dots, \tilde{T}_{\tilde{g}}\}$.

3.3. Implementation of the hole-filling method

During the optimization, the evolution of structural topology is a process of gradually generating and merging cavities and tunnels. The basic idea of the hole-filling method is to control the element update scheme to satisfy

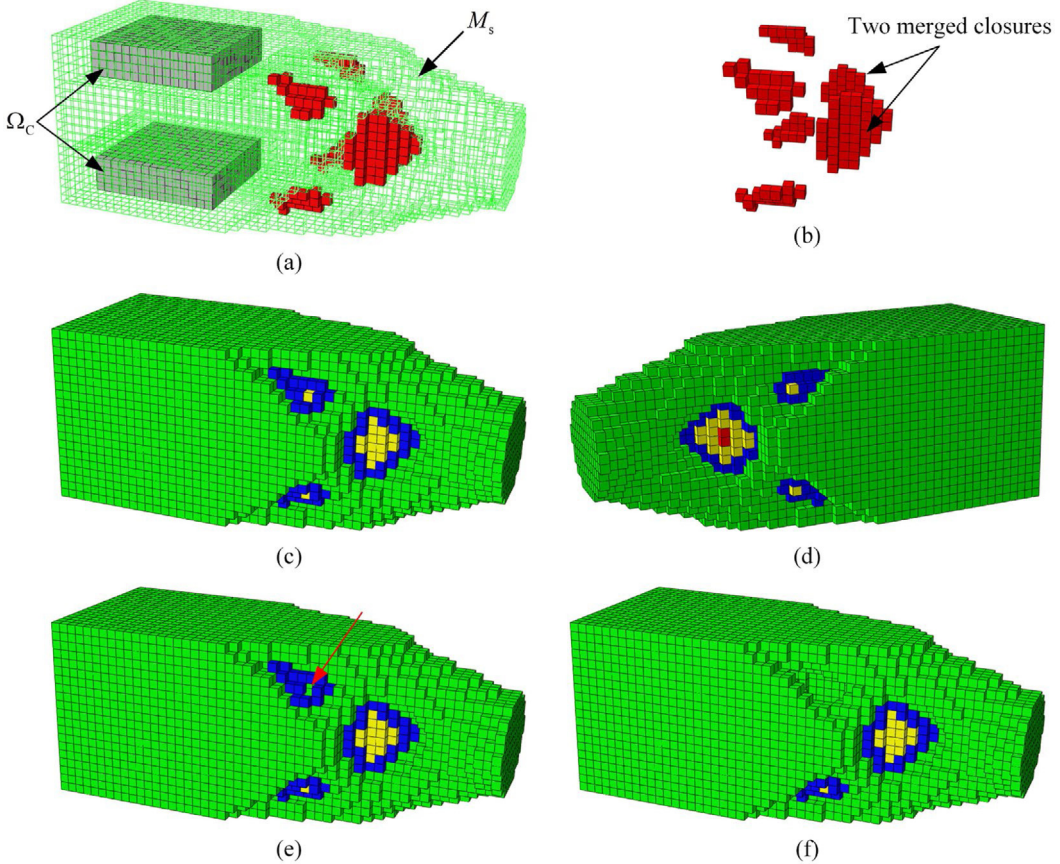


Fig. 9. Identification of each tunnel closure in a topological hull. (a) The topological hull of a structure $\Theta(M_s)$. (b) The set difference between $\Theta(M_s)$ and $M_s \cup \Omega_C$. (c) and (d) is the distance transform of Ω_T using the chessboard distance. Blue voxels, yellow voxels, and red voxels are considered the distance of 1, 2, and 3 from the structure, respectively. (e) Topological hull with one regional maximum removed $\Theta(M_s) \setminus M_{\max}^e$. The red arrow points out the removed voxel of a regional maximum M_{\max}^e . (f) Topological hull of M_s with one tunnel closure removed. (For interpretation of the references to color in this figure legend, the reader is referred to the web version of this article.)

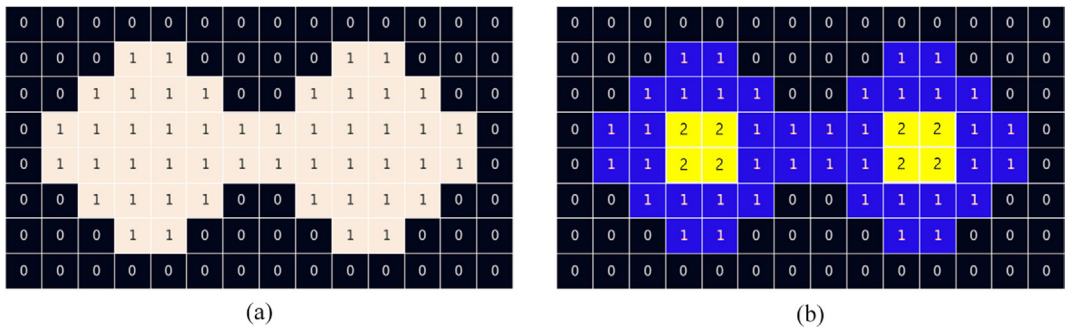


Fig. 10. An example of a tunnel closure with two regional maxima. (a) A binary model with one tunnel closure (white voxels) and solid voxels M_s (black voxels). (b) Distance transform of the tunnel with two regional maxima (yellow voxels). (For interpretation of the references to color in this figure legend, the reader is referred to the web version of this article.)

the topological constraints. Before the material volume reaches the target value V^* , the SCC approach divides the design variable update in each iteration into two sub-steps. In the first sub-step, the number of existing cavities and tunnels of the current structure is constrained to be fewer than or equal to the target number [see Eqs. (2a) and (2b)]. Since the hole-filling method may add solid elements to close excess cavities or tunnels, the volume of material may not meet the target volume constraint [see Eq. (8)]. To precisely satisfy the volume constraint, a certain number of elements with lower structural efficiency will be deleted from the structure in the second sub-step.

In the first sub-step, the element update is first carried out according to the sensitivity threshold (see Section 2). In this step, new cavities and tunnels are generated. As mentioned in Section 3.1.2, the simple points are the elements that do not alter structural topology. Therefore, elements that are not simple points are not allowed to be re-admitted into the structure to avoid self-closing cavities or tunnels. Then, the structural topology of the updated structure can be directly controlled by closing the excess cavities and tunnels with the corresponding closures. In this work, the size of each cavity (denoted as S_j^C) or each tunnel (denoted as S_k^G) is measured by the cardinality of its closure, denoted as $|\tilde{O}_i|$ or $|\tilde{T}_i|$. It is assumed that, compared with closing a larger cavity or tunnel, closing a smaller one will result in a smaller change in the objective function. Thus, during the evolutionary process, the closures of existing cavities $\Omega_C^* = \{\tilde{O}_1, \tilde{O}_2, \dots, \tilde{O}_{\tilde{c}}\}$ and tunnels $\Omega_T^* = \{\tilde{T}_1, \tilde{T}_2, \dots, \tilde{T}_{\tilde{g}}\}$ are calculated, and the smaller cavities and tunnels will be closed if the topological constraint is violated. As mentioned above, the element sets of Ω_C^* and Ω_T^* are both arranged in ascending order. Thus, the formulation of the hole-filling method is expressed as

$$x_i = \begin{cases} x_{\min}, & \text{if } \tilde{c} \leq \tilde{C} \text{ and } \tilde{g} \leq \tilde{G}, \tilde{v}_i \in \left\{ \bigcup_{j=1}^{\tilde{c}} \tilde{O}_j \right\} \cup \left\{ \bigcup_{k=1}^{\tilde{g}} \tilde{T}_k \right\} \\ 1, & \text{if } \tilde{c} > \tilde{C} \text{ and } \tilde{g} \leq \tilde{G}, \tilde{v}_i \in \left\{ \bigcup_{j=1}^{\tilde{c}-\tilde{C}} \tilde{O}_j \right\} \\ 1, & \text{if } \tilde{c} \leq \tilde{C} \text{ and } \tilde{g} > \tilde{G}, \tilde{v}_i \in \left\{ \bigcup_{k=1}^{\tilde{g}-\tilde{G}} \tilde{T}_k \right\} \\ 1, & \text{if } \tilde{c} > \tilde{C} \text{ and } \tilde{g} > \tilde{G}, \tilde{v}_i \in \left\{ \bigcup_{j=1}^{\tilde{c}-\tilde{C}} \tilde{O}_j \right\} \cup \left\{ \bigcup_{k=1}^{\tilde{g}-\tilde{G}} \tilde{T}_k \right\} \end{cases} \quad (20)$$

where \tilde{v}_i is the i th element (or voxel) in the design domain, and x_i is its corresponding design variable.

In the second sub-step, a topology-preserving method is adopted to perform shape optimization [20]. The core of the topology-preserving method is to update the boundary elements ∂M_s which are identified as simple points to maintain the invariance of the structural topology. Thus, the volume constraint in each iteration can be satisfied while the number of cavities and tunnels can be preserved from the first sub-step. For any element v_i , it belongs to the boundary elements ∂M_s if one of the following conditions is satisfied:

$$M_s \cap N_{26}(\tilde{v}_i) \neq \emptyset \text{ and } M_e \cap N_{26}(\tilde{v}_i) \neq \emptyset \quad (21)$$

$$\tilde{v}_i \in \partial \Omega \text{ and } \tilde{v}_i \in M_s \quad (22)$$

The above update scheme continues until the target volume fraction is reached. Once the volume of material reaches the target value V^* , only shape optimization will be conducted in the following iteration. To control the size of the cavities and tunnels, the element removal is first carried out in the neighborhood of each closure of the existing cavity or tunnel. The neighborhood of each closure is defined as

$$\partial \tilde{O}_j = \left\{ \tilde{v}_i \mid d_{26}(\tilde{v}_i, \tilde{O}_j) \leq 1 \right\} \cap M_s \quad (23a)$$

$$\partial \tilde{T}_k = \left\{ \tilde{v}_i \mid d_{26}(\tilde{v}_i, \tilde{T}_k) \leq 1 \right\} \cap M_s \quad (23b)$$

where $\partial \tilde{O}_j$ and $\partial \tilde{T}_k$ denote the neighborhood elements of the corresponding cavity and tunnel, respectively. As shown in Fig. 11, one can easily obtain the neighboring solid elements of each closure using Eq. (23b). The topology-preserving method is performed iteratively in each closure and its neighborhood until the following to

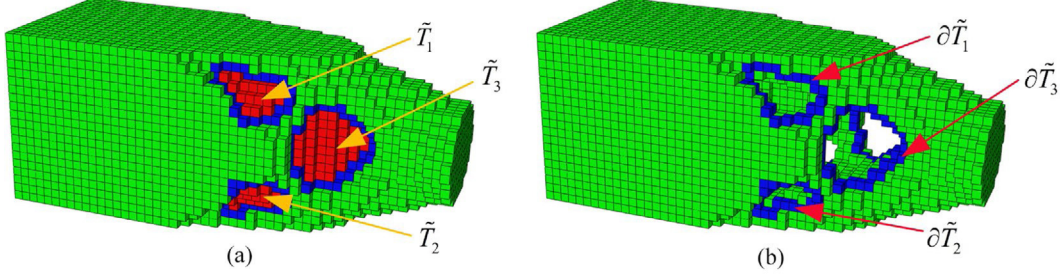


Fig. 11. Identification of neighboring solid elements of tunnel closures. (a) Solid structure M_s with several tunnel closures (highlighted in red). (b) Solid structure M_s without any closure and the corresponding neighborhood of each closure (highlighted in blue). (For interpretation of the references to color in this figure legend, the reader is referred to the web version of this article.)

conditions are satisfied:

$$S_j^{\tilde{c}} = \sum_{\tilde{v}_i \in \tilde{\Omega}_j \cup \partial\tilde{\Omega}_j} v_i(1 - x_i) \geq S_*^{\tilde{c}} \quad (24a)$$

$$S_k^{\tilde{G}} = \sum_{\tilde{v}_i \in \tilde{T}_k \cup \partial\tilde{T}_k} v_i(1 - x_i) \geq S_*^{\tilde{G}} \quad (24b)$$

where the iteration variables j and k increase from 1 to \tilde{g} and from 1 to \tilde{c} , respectively. In the above process, new closures for the current structure will be updated for the following iteration. Thus, the neighboring elements of each tunnel will be gradually removed to meet the size constraint (see Fig. 11b). If the size constraint is not specified, the element update will be carried out on the boundary elements ∂M_s to conduct shape optimization.

3.4. Minimum length scale control

The minimum length scale of the structural members is precisely controlled with the help of the structural skeleton. A graphic thinning algorithm is employed to obtain the structural skeleton by gradually removing simple points from the structural boundary layer by layer [77]. The minimum length scale of the structural members can be directly controlled by restricting the distance between the structural boundary and the skeleton. This can be realized by imposing a circular or a spherical region with a predetermined diameter R_t along the skeleton M_{sk} and the elements that are swept in the circle or sphere are set as non-designable by prescribing their design variables to be 1, i.e.,

$$x_i = 1, i \in \{\tilde{v}_i | d(\tilde{v}_i, M_{sk}) \leq R_t\} \quad (25)$$

Implementing the above length scale constraint can prevent thin parts of the structure from being filtered out and therefore avoid reducing the number of cavities and tunnels. For the equality constraint [see Eq. (2b)], the minimum length scale control of the structural members should be implemented in all iterations. For the inequality constraint [see Eq. (2a)], we can remove the length scale control when doing the optimization. The different constraints will be demonstrated in the numerical examples.

In addition to the minimum length scale control of the structural members, some sheet-like features may be generated in the structure, because the hole-filling method will generate one-voxel-thick patches to cover the unwanted tunnels. As shown in Fig. 12a, it is insufficient to use the structural skeleton alone to control the minimum length scale of these sheet-like components. These one-voxel-thick elements cannot be removed when doing the shape optimization, as their removal will generate new tunnels and change the structural topology (see Fig. 12b and c). Thus, we propose a simple method to control the minimum thickness of the thin sheet components. The two-dimensional isthmuses will be identified as thin sheet components M_{sheet} , which can be easily obtained by checking the topological numbers of each element. Similar to the length scale control of the structural members, a spherical region with a radius of R_t is introduced for any element $\tilde{v}_i \in M_{sheet}$. Any elements within the spherical region will be defined as solid elements, i.e.,

$$x_i = 1, i \in \{\tilde{v}_i | d(\tilde{v}_i, M_{sheet}) \leq R_t\} \quad (26)$$

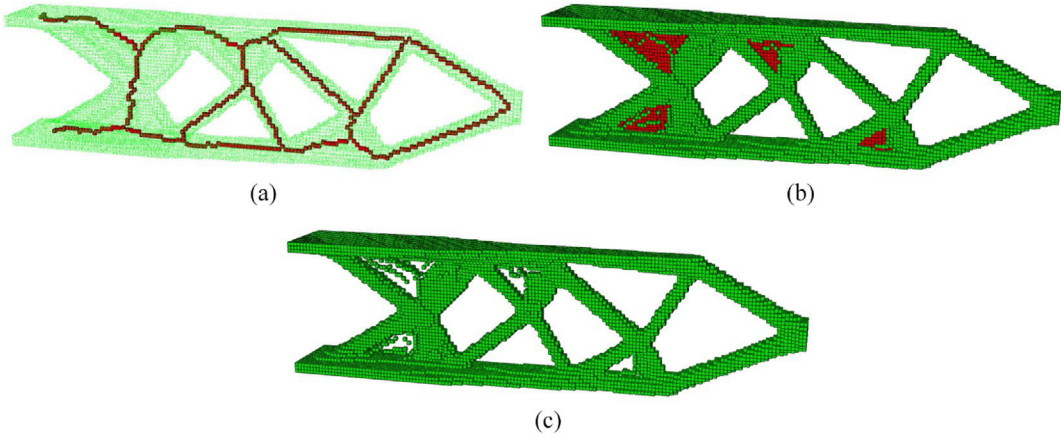


Fig. 12. Controlling the minimum thickness of sheet-like components. (a) Solid structure M_s with its structural skeleton (highlighted in red). (b) two-dimensional isthmuses (highlighted in red). (c) New tunnels are generated after removing the two-dimensional isthmuses. (For interpretation of the references to color in this figure legend, the reader is referred to the web version of this article.)

It should be noted that the minimum thickness control of the sheet-like components is only employed when the volume fraction reaches V^* . Thus, the length scale control of the thin sheets will not interfere with the hole-filling process. If we remove the thickness constraint, the minimum thickness of the sheet-like components is equal to the length scale of the element size.

3.5. Evolutionary procedure for the SCC approach

The numerical implementation procedure of the SCC approach is described as follows.

Step 1. Discretize the design domain using a structured hexahedral grid and assign material property (1 or x_{\min}) to each element to construct an initial design. For the inequality constraint [see Eq. (2a)], the optimization can start from the initial full design. For the equality constraint [see Eq. (2b)], the optimization should start with an initial design (or start from the n th iteration) where the numbers of cavities and tunnels are equal to or greater than the target values.

Step 2. Carry out finite element analysis and calculate elemental sensitivities using Eq. (7).

Step 3. Obtain the structural skeleton M_{sk} of the current design using the thinning algorithm [77].

Step 4. Update the design variable based on the ranking of elemental sensitivities and the target material volume $V^{(n)}$, as defined in Eq. (8). In this step, elements that are not simple points are prohibited from being reintroduced into the structure to prevent self-closing cavities or tunnels. Moreover, the element update should follow the minimum length scale control according to Eq. (25).

Step 5. Implement the hole-closing algorithm (as described in Table 3) on the updated structure M_s to obtain the topological hull $\Theta(M_s)$.

Step 6. Identify the number of distinct closures for cavities and tunnels within the structure M_s based on its topological hull $\Theta(M_s)$, as demonstrated in Section 3.2.

Step 7. Perform the hole-filling method according to Eq. (20) to meet the topological constraint.

Step 8. Shape optimization is conducted using the topology-preserving method [20]. In each iteration, update the new structural skeleton M_{sk} and apply minimum length scale control according to Eq. (25).

Step 9. Repeat Steps 2 to 8 until the target volume V^* is reached.

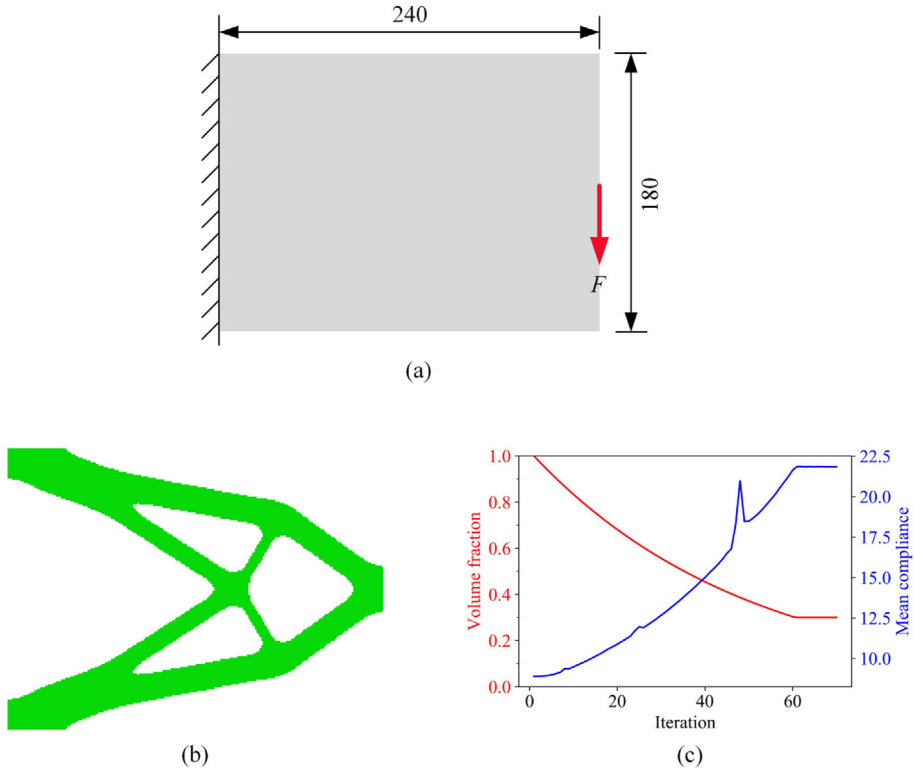


Fig. 13. Example of the two-dimensional cantilever beam. (a) Loading and boundary conditions of the cantilever beam. (b) The initial optimized design without SCC. (c) Evolution histories of the volume fraction and mean compliance.

Step 10. Conduct shape optimization according to Eqs. (24a) and (24b). In each iteration, update the new structural skeleton M_{sk} and thin sheet components M_{sheet} , and apply minimum length scale control according to Eqs. (25) and (26).

Step 11. Repeat Step 10 until the convergence criterion in Eq. (9) is satisfied.

4. Numerical examples

In this section, three typical optimization problems are used to verify the effectiveness of the developed approach for SCC. The SCC approach is implemented through a Python code that links to Abaqus. The Python code can read the initial design with an arbitrarily-shaped geometry from a model database (.inp file), and it can take advantage of the sophisticated FEA capabilities of the Abaqus software. In all examples, it is assumed that the material is homogeneous, isotropic, and linearly elastic. The design domains are discretized using eight-node hexahedral elements. The Young's modulus and Poisson's ratio are $E = 1$ and $\nu = 0.3$, respectively. The compliance ratios of the optimized designs with and without SCC are compared to illustrate the effectiveness of the proposed approach. Moreover, Altair Inspire's PolyNURBS tools are used to smooth the three-dimensional optimized designs to generate a visually appealing computer-aided design model.

4.1. Two-dimensional cantilever beam

The first example considers a two-dimensional cantilever beam. Fig. 13a shows the loading and boundary conditions of the optimization problem. The concentrated force $F = 1$ is applied at the middle of the free end. The design domain is discretized into 240×180 elements. The target volume fraction and the filter radius are 30% and 12, respectively. The minimum length scale constraint R_t for the SCC is 5 [see Eq. (25)].

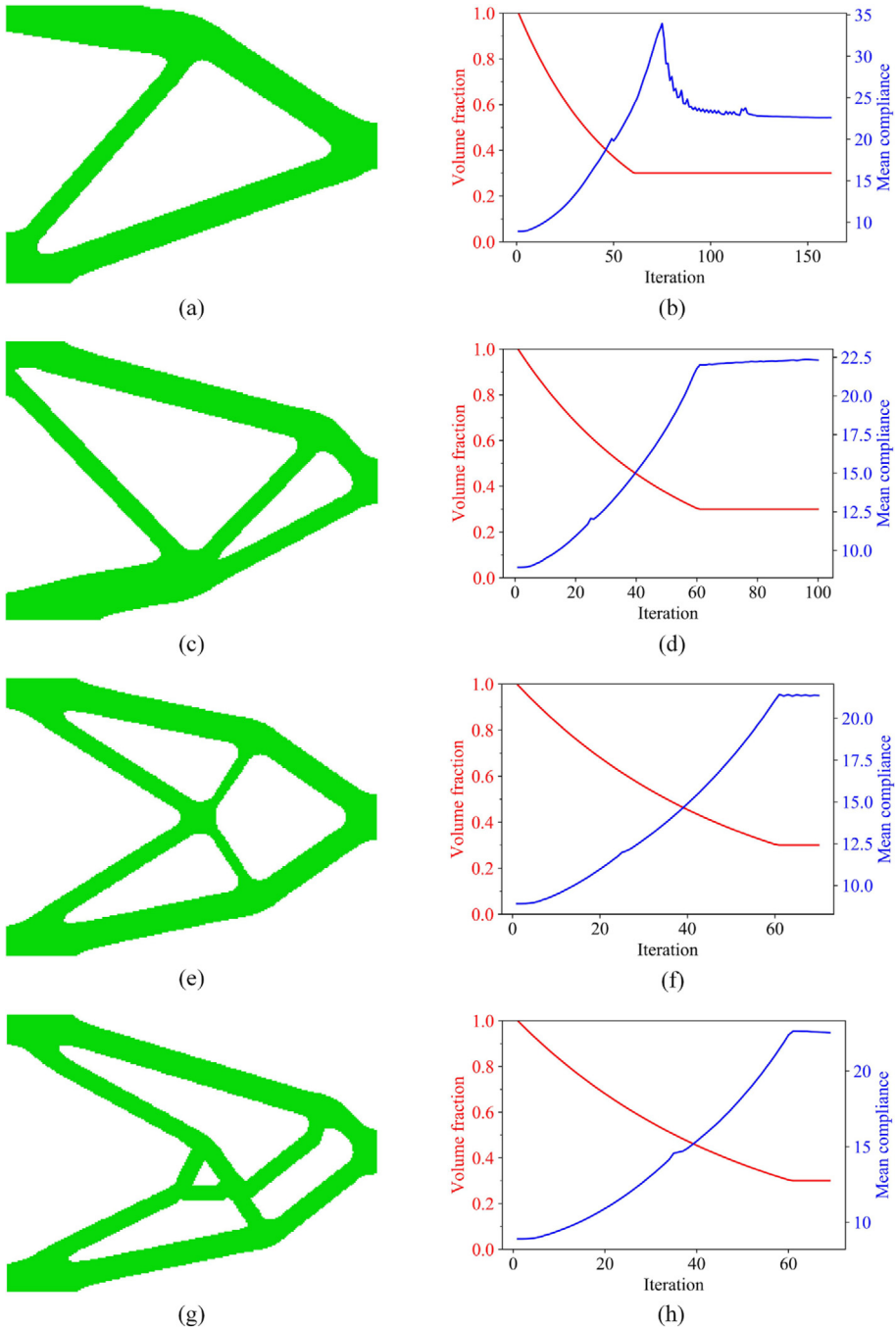


Fig. 14. Optimized design with SCC. (a), (c), (e), and (g) are the optimized designs whose target numbers of cavities are one, two, three, and four, respectively. The evolution histories of the volume fraction and mean compliance of each case are plotted in (b), (d), (f), and (h), respectively.

The standard BESO optimization without the SCC is first performed. Fig. 13b shows the initial optimized (IO) design of the two-dimensional cantilever beam. The final structure consists of three cavities, which form an X-shaped component in the middle. The evolution histories of the volume fraction and mean compliance are plotted in Fig. 13c.

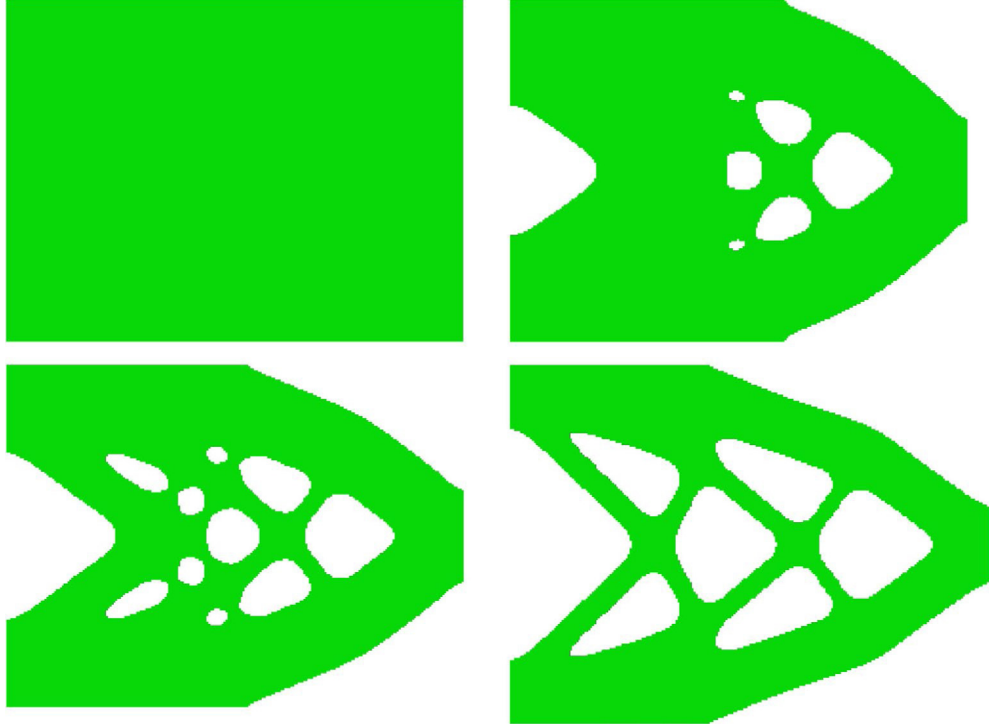


Fig. 15. Evolution history of a cantilever beam without SCC. The target volume fraction is 50%.

The structural optimization with the SCC is then investigated. Fig. 14a, Fig. 14c, Fig. 14e, and Fig. 14g show the optimized designs with different target numbers of cavities \tilde{C} . The evolution histories of the volume fraction and mean compliance of each case are plotted in Fig. 14b, Fig. 14d, Fig. 14f, and Fig. 14h, respectively. In the case shown in Fig. 14a, the minimum size of the cavity is required not to be less than 20% of the volume of the design domain V . In both cases shown in Fig. 14c and Fig. 14e, the minimum volume of each cavity is set as 2% of the design domain V . For the case in Fig. 14g, there is no constraint on the minimum size of the cavities. Due to the topological constraints, the optimized designs of cases in Fig. 14a and Fig. 14c are distinctly different from the IO design (Fig. 13b). However, the structural compliances only increase by 4% and 2%, respectively. As the target number of cavities in the case in Fig. 14e is equal to the cavity number of the IO design, there is a strong resemblance between this case and the IO design (Fig. 13b). The structural compliance of the case in Fig. 14e is even 2% lower than the IO design (Fig. 13b). The reason may be that the shape of the structural layout is optimized at the end of each iteration. Since there is no constraint on the minimum size of the cavities in the case in Fig. 14g, one cavity is degenerated into a small one to form a big “triangular node” in the middle of the structure. Compared with the IO design (Fig. 13b), the increment of structural compliance in this case is 3%. The results of this numerical example show that the proposed SCC approach is capable of relocating structural cavities to achieve the most efficient structural layout.

All the above cases start from the full design with no initial cavities or tunnels. However, during the optimization process, the number of newly generated cavities might be lower than the target value, resulting in the inequality constraint [see Eq. (2a)]. Fig. 15 shows part of the evolution histories of a cantilever beam and its IO design without the SCC, where the target volume fraction is 50%. The peak value of the number of cavities is 10. In order to apply the equality constraint [see Eq. (2b)] with a higher target value (larger than 10), the SCC approach should start from an initial design whose number of cavities is equal to or greater than the target numbers.

In the next three cases, the influence of the distribution of initial cavities on structural optimization is investigated. The target volume fraction is 50% for the following three cases. In the first case (see Fig. 16a), $13 \times 7 = 91$ cavities are evenly distributed in the initial design (highlighted in red). In the next two cases, we start the SCC from two random initial designs. As shown in both Fig. 17a and Fig. 18a, we randomly create 200 cavities in the

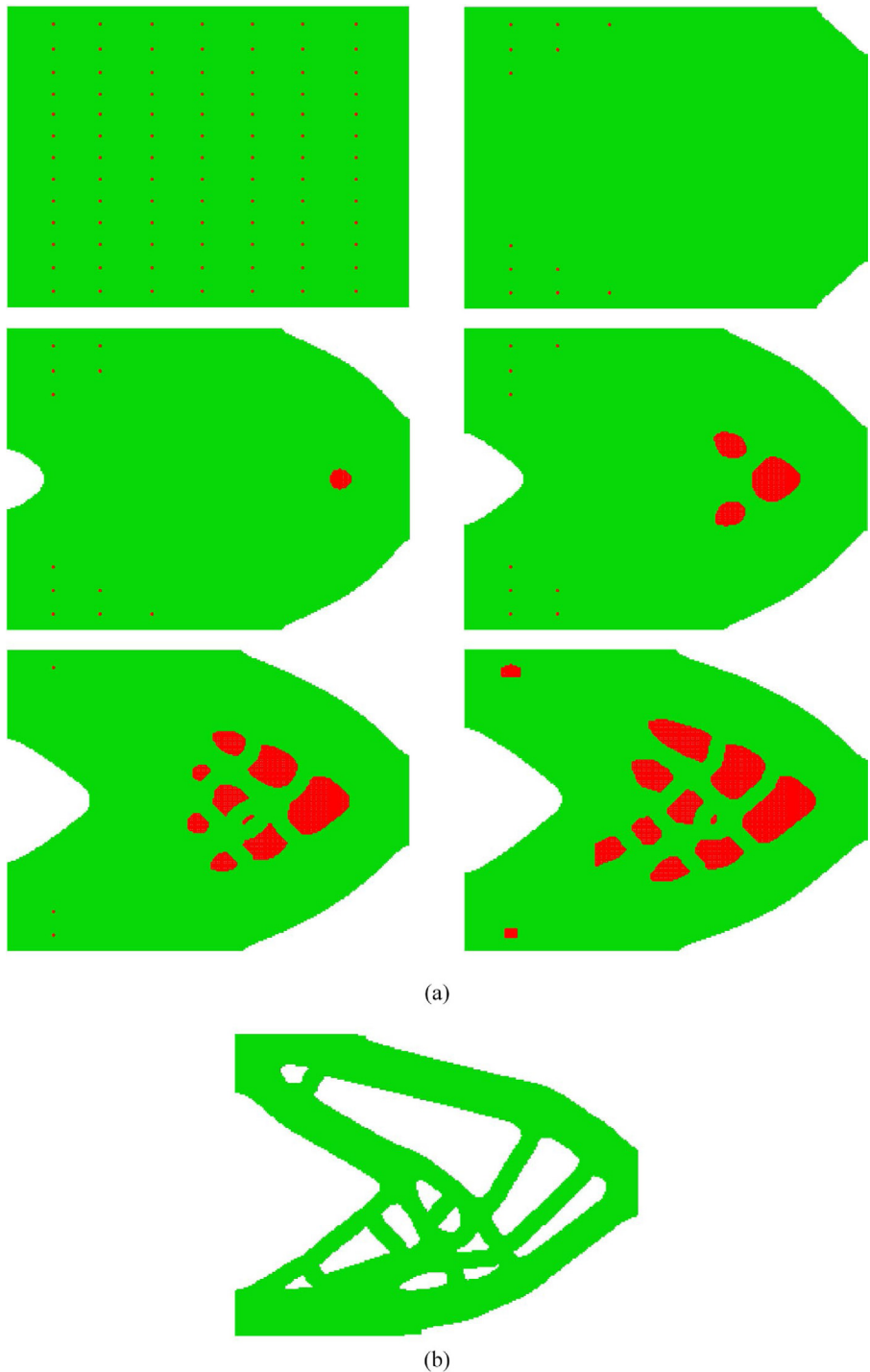


Fig. 16. Influence of initial design on optimized design. (a) Initial design with a prescribed number of cavities and evolution history (cavities are highlighted in red). (b) Optimized design with SCC. (For interpretation of the references to color in this figure legend, the reader is referred to the web version of this article.)

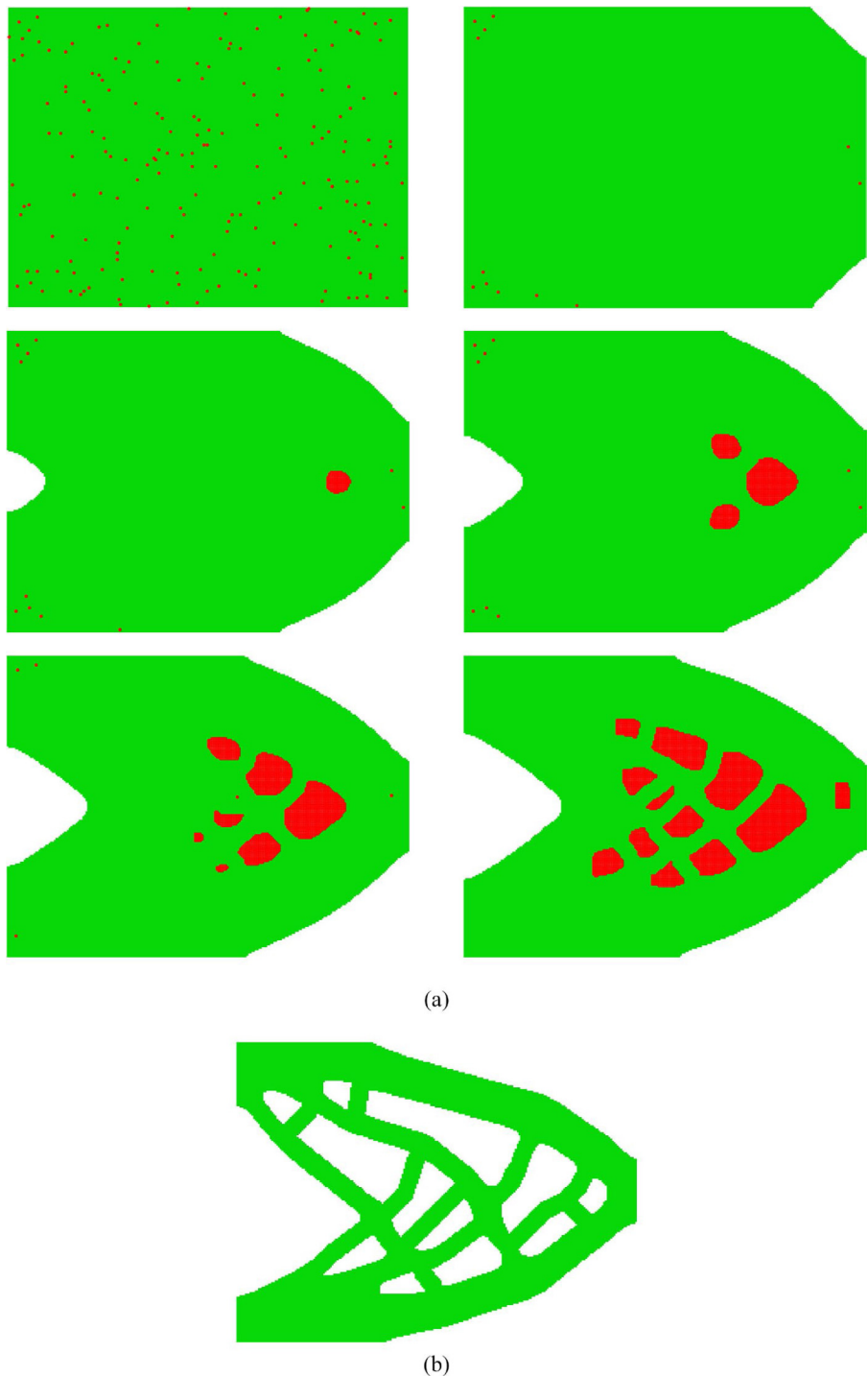


Fig. 17. Influence of initial design on optimized design. (a) Initial design with a prescribed number of cavities and evolution history (cavities are highlighted in red). (b) Optimized design with SCC. (For interpretation of the references to color in this figure legend, the reader is referred to the web version of this article.)

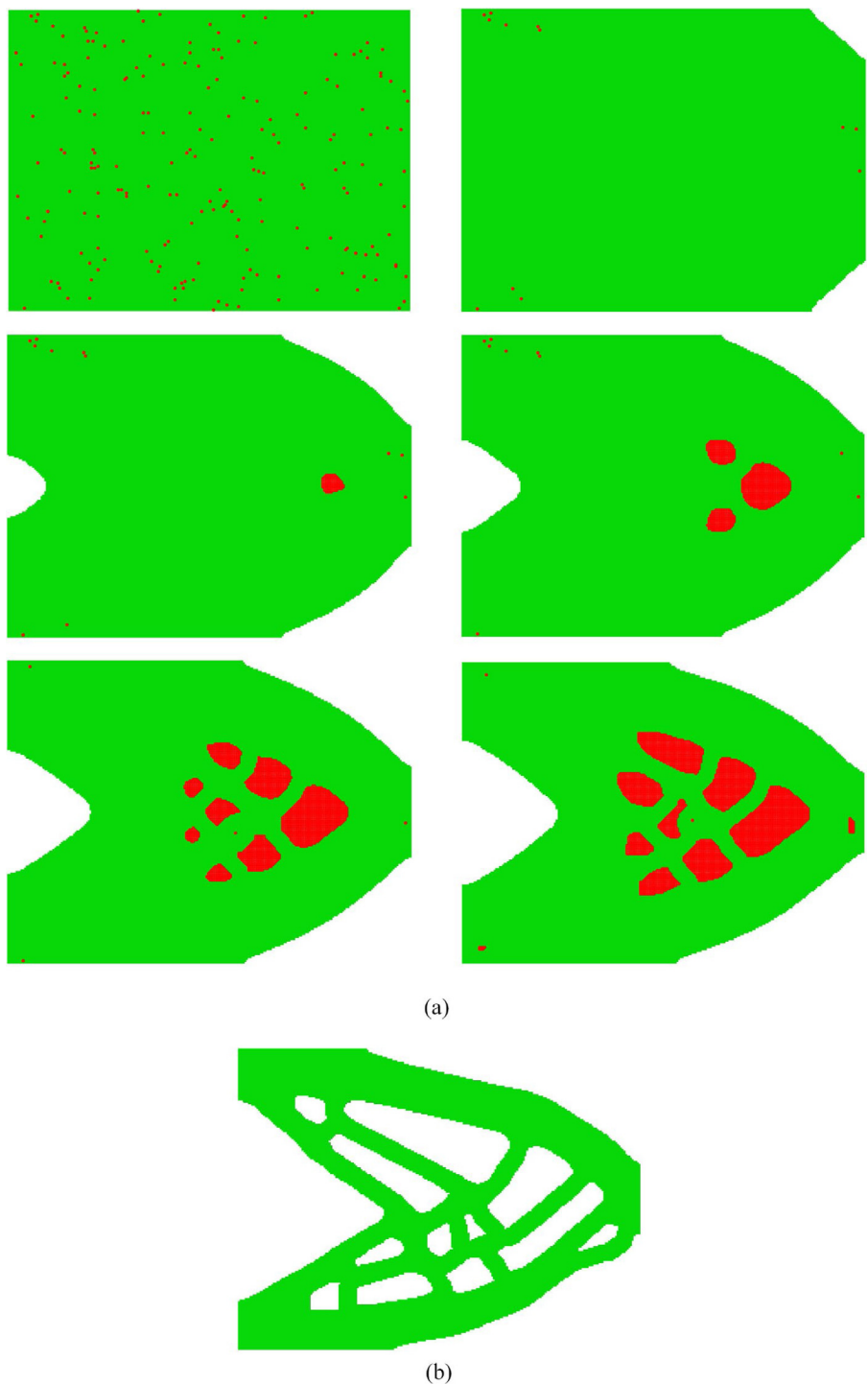


Fig. 18. Influence of initial design on optimized design. (a) Initial design with a prescribed number of cavities and evolution history (cavities are highlighted in red). (b) Optimized design with SCC. (For interpretation of the references to color in this figure legend, the reader is referred to the web version of this article.)

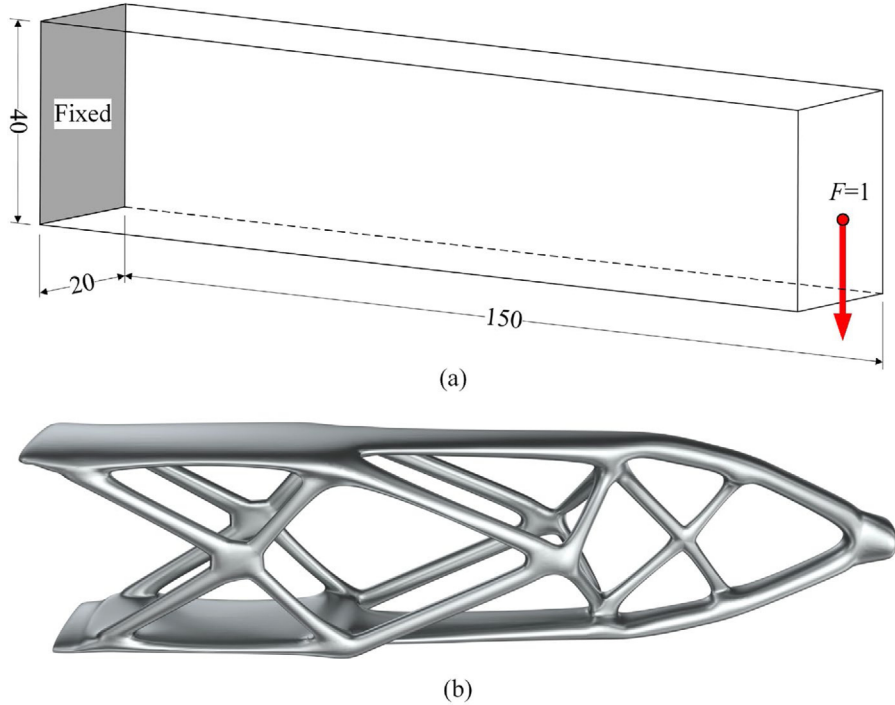


Fig. 19. Example of the three-dimensional cantilever beam. (a) Loading and boundary conditions of the cantilever beam. (b) The initial optimized design without SCC.

initial structure. The target number of cavities \tilde{C} is 12 for each case. Fig. 16a, Fig. 17a, and Fig. 18a show the evolution process of the distribution of the existing cavities in the structure for each case. Fig. 16b, Fig. 17b, and Fig. 18b present the final optimized design of each case. It can be seen that the equality constraint is achieved during the whole form-finding process. Although the re-distribution of cavities during the optimization process is quite different, the number of existing cavities remains constant at 12 to meet the target value. It should be noted that the optimization process of the BESO method is highly related to the sensitivity history of each element [see Eq. (7)]. Thus, the structural layout of the optimized design is highly dependent on the choices of the initial design. In comparison to the IO design (Fig. 15), the compliance of the optimized design increases by 4% for Fig. 16b, 3% for Fig. 17b, and 5% for Fig. 18b. The results suggest that the SCC approach is able to provide a series of diverse design options that have highly competitive structural performance.

4.2. Three-dimensional cantilever beam

In the second example, we consider a three-dimensional cantilever beam. The loading and boundary conditions are shown in Fig. 19a. The design domain is discretized by a $150 \times 40 \times 20$ finite element mesh. The concentrated force that acts on the beam is set as $F = 1$. Three layers of elements on the free end are prescribed as non-designable. The target volume fraction and the filter radius are 15% and 3, respectively. The minimum length scale constraint for the structural members is $R_t = 1$ [see Eq. (25)]. The thickness constraint for the sheet-like components is only applied in case Fig. 20c [see Eq. (26)]. The minimum volumes of each cavity and tunnel are set as 2% and 0.2% of the design domain, respectively.

Structural optimization of the 3D cantilever beam without the SCC is first investigated. Fig. 19b shows the IO design of the 3D cantilever beam. As can be seen, it has 15 tunnels which form a V-shaped outer frame and several X-shaped members. The final design is similar to a spatial truss structure.

The structural optimization of the 3D cantilever beam example with the SCC is then investigated. Fig. 20a shows the optimized design with the target number of tunnels $\tilde{T} = 0$ and cavities $\tilde{C} = 0$. In this case, the minimum

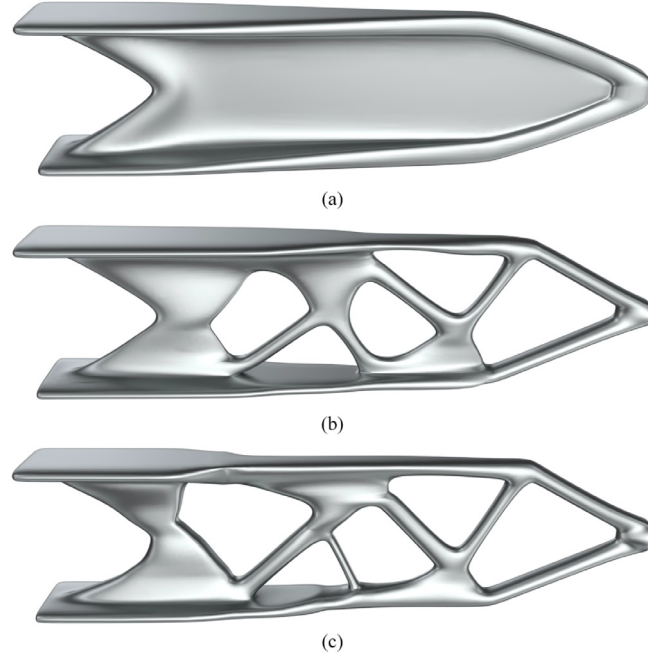


Fig. 20. Optimized designs of the three-dimensional cantilever beam with SCC. (a) Optimized design with $\tilde{T} = 0$ and $\tilde{C} = 0$. (b) Optimized design with $\tilde{T} = 5$ and $\tilde{C} = 0$. (c) Optimized design with $\tilde{T} = 5$ and $\tilde{C} = 0$. In this case, the minimum thickness of the sheet-like component is set as 3 ($R_t = 1$).

thickness control of the sheet-like component is not applied. Thus, the minimum thickness of the thin sheet is equal to 1 which is the length scale of the element. The structural compliance of the case shown in Fig. 20a is 7% lower than the IO design (Fig. 19b). It shall be noted that, for stiffness optimization, sheet-like or closed-walled structures are much stiffer than Michell-like structures [63]. Thus, by generating sheet-like patches to constrain the number of tunnels, the structural performance can be improved. Fig. 20b shows the optimized design with $\tilde{T} = 5$ and $\tilde{C} = 0$. The compliance value of this case is 3% lower than that of the IO design (Fig. 19b). The increment of structural compliance compared to the case in Fig. 20a further indicates that the frame restriction from the length scale control may result in lower structural performance. In the third case of the 3D cantilever, the influence of the thickness constraint of the sheet-like components on structural optimization is studied. Fig. 20c shows the structural layout of the optimized design with $\tilde{T} = 5$ and $\tilde{C} = 0$. In this case, R_t is set as 1 for Eq. (26). Due to the thickness constraint, the sheet-like components in Fig. 20c are noticeably thicker than those in Fig. 20b. Compared to the case in Fig. 19b, the compliance of the case in Fig. 20c increases by 1%. Therefore, comparing cases Fig. 20b and Fig. 20c, removing the thickness constraint might increase the structural stiffness.

The influence of removing the length scale constraint of the structural members on the SCC is investigated by comparing the cases shown in Figs. 21 and 22. In the two cases, $\tilde{T} = 10$ and $\tilde{C} = 0$. Different from the case in Fig. 21, the length scale constraint of the structural members [Eq. (25)] is not applied to the first sub-step of every iteration in the case in Fig. 22. As shown in Fig. 21a, due to the length constraint, the structural members cannot be disconnected but can be relocated in the structure, thereby achieving the equality constraint on the number of tunnels (see Fig. 21b). However, Fig. 22a shows that removing the length scale constraint of the structural members can result in merging of the tunnels. Thus, inequality constraints may occur if we remove the length scale constraint for the members. Applying inequality constraints is practically useful in design scenarios when only the maximum number of tunnels or cavities need to be controlled to reduce manufacturing costs. Moreover, this strategy can effectively generate alternative structural forms, which is beneficial for designers in architecture or other related fields. As shown in Fig. 22b, although the target number of tunnels is 10, the number of tunnels in the final design is 9. The structural compliances of the cases in Fig. 21b and Fig. 22b are 3% lower than that of the IO design (Fig. 19b).

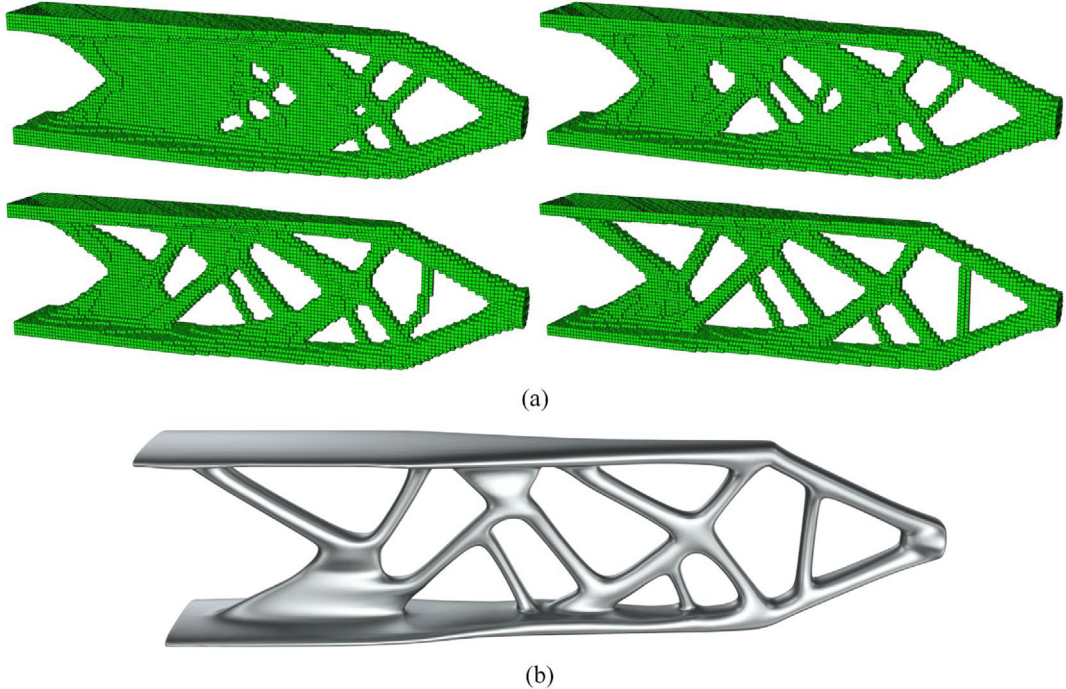


Fig. 21. Optimized designs of the three-dimensional cantilever beam with SCC. (a) Evolution history. (b) Optimized design with $\tilde{T} = 10$ and $\tilde{C} = 0$.

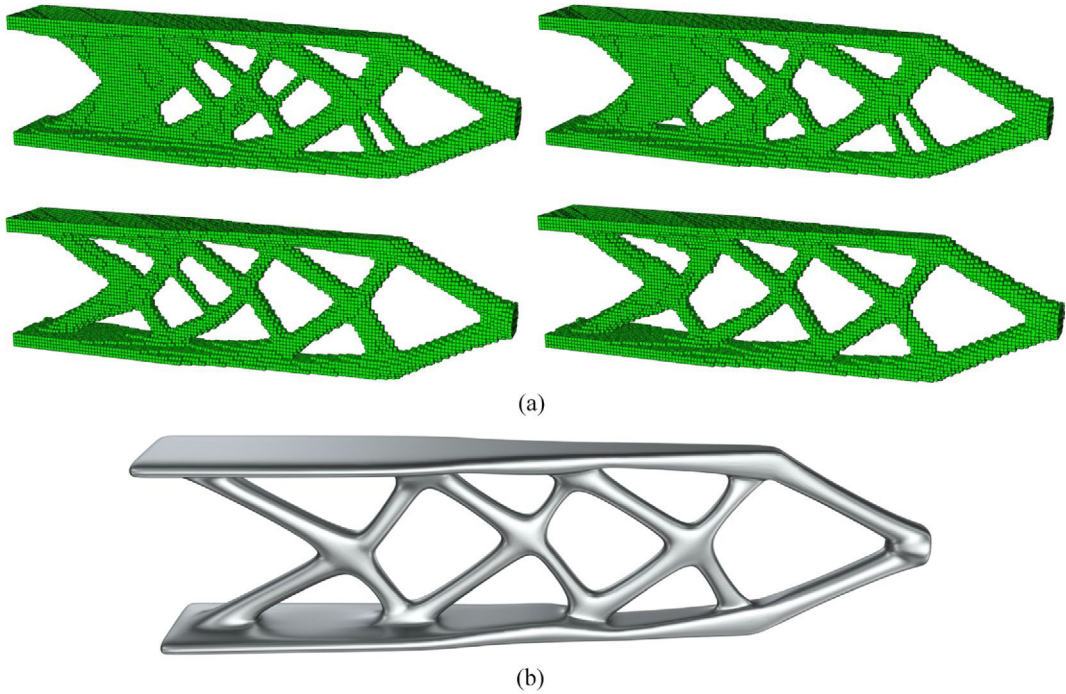


Fig. 22. Optimized designs of the three-dimensional cantilever beam with SCC. (a) Evolution history. In this case, the minimum length scale control of the structural members is not considered in the first sub-step of each iteration. (b) Optimized design with $\tilde{T} = 10$ and $\tilde{C} = 0$.

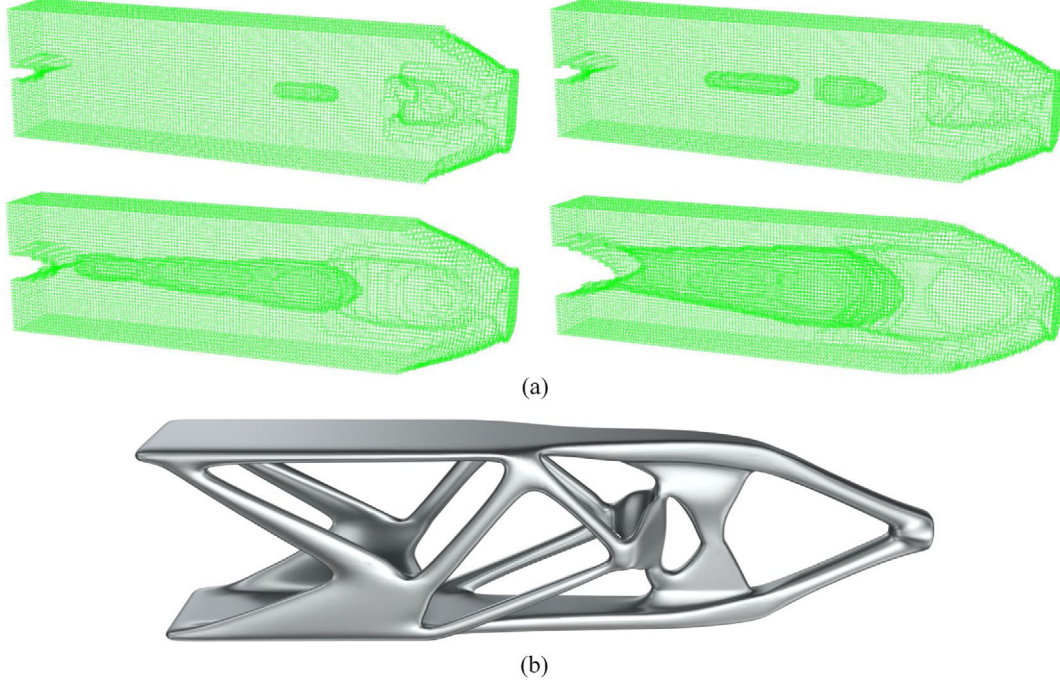


Fig. 23. Optimized designs of the three-dimensional cantilever beam with SCC. (a) Evolution history. In this case, the minimum length scale control of the structural members is not considered in the first sub-step of each iteration. (b) Optimized design with $\tilde{T} = 10$. The number of cavities is not constrained in this case.

In the above cases, the number of cavities is strictly controlled with $\tilde{C} = 0$. Fig. 23b shows the optimized design by only specifying the genus constraint $\tilde{T} = 10$. Fig. 23a shows the optimization process in this case. The generation and reduction of cavities are allowed during the entire optimization process. In comparison to the structure in Fig. 19b, the increments of compliance are only 3%. The results show that alternative design solutions can be generated in this way.

In the following cases, we will demonstrate the strategy for applying the SCC to different sub-regions of the design domain. Fig. 24c shows the optimized design obtained by only imposing the genus constraint in the red region in Fig. 24a, and the target number of tunnels in the red region is $\tilde{T} = 5$. As shown in Fig. 24b, the target number of tunnels in the yellow, blue, and red regions are $\tilde{T} = 2$, $\tilde{T} = 4$, and $\tilde{T} = 5$, respectively. Fig. 24d shows the optimized design by applying the SCC in multiple sub-regions of the design domain. Compare with the structure in Fig. 19b, the compliance of the optimized structure only increases by less than 1% for the case in Fig. 24c and 2% for the case in Fig. 24d.

In the last two cases, both the cavities and tunnels are constrained. In the following cases, the target volume fraction is 35%. Fig. 25a presents the IO design of the 3D cantilever. Fig. 25b shows the two selected sub-regions. In Fig. 25c, $\tilde{C} = 3$ and $\tilde{T} = 3$ are specified in the white and red regions, respectively. In Fig. 25d, $\tilde{C} = 2$ and $\tilde{T} = 4$ are specified in the white and red regions, respectively. Compared to the case shown in Fig. 25a, the increments of structural compliance are 5% in Fig. 25c and 8% in Fig. 25d. In general, regional SCC control can be precisely realized, and the structural efficiency can be guaranteed.

4.3. Three-dimensional cantilever beam under torsion

In the third example, a three-dimensional cantilever beam under torsion is considered. The design domain and boundary conditions are shown in Fig. 26a. A torque is applied on the free end. The design domain is discretized by a mesh with $180 \times 60 \times 60$ elements. Only a quarter of this model is optimized due to symmetry. The target volume fraction is 15% for all the following cases. The minimum length scale constraint for the structural members is $R_t = 1$ [see Eq. (25)]. The minimum volume of each tunnel is set as 0.2% of the design domain.

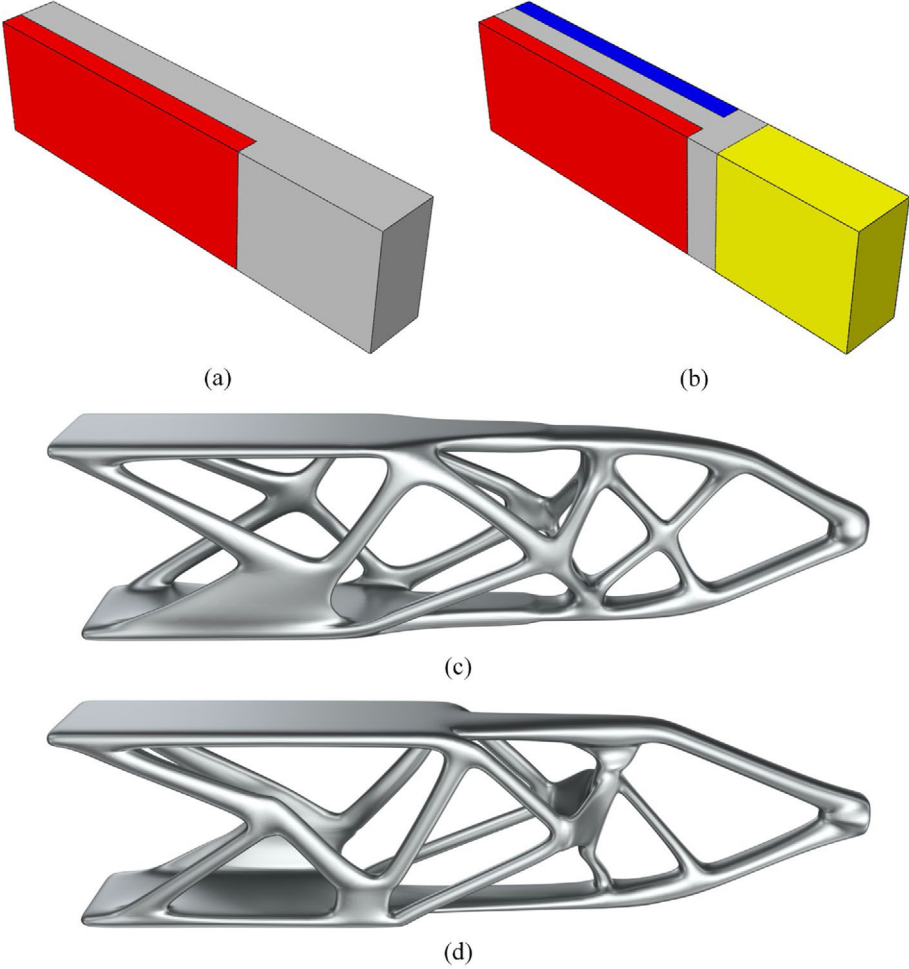


Fig. 24. Impose SCC in selected sub-regions. (a) $\tilde{T} = 5$ for the red region. (b) $\tilde{T} = 2$, $\tilde{T} = 4$, and $\tilde{T} = 5$ for yellow, blue, and red regions, respectively. The optimized designs (c) and (d) are evolved from (a) and (c), respectively. (For interpretation of the references to color in this figure legend, the reader is referred to the web version of this article.)

[Fig. 26b](#) and [Fig. 26c](#) demonstrate the IO design without the SCC. In this case, the filter radius is set as 3. [Fig. 26d](#) and [Fig. 26e](#) show the IO design without the SCC, in which the filter scheme is switched off. The optimized design of [Fig. 26e](#) is 20% stiffer than the structure in [Fig. 26c](#). The low performance of the design in [Fig. 26c](#) is because of the imposed length scale of the filter scheme. The filter scheme will impose solid material to stay closer to the centerline of the design domain.

[Fig. 27a](#) and [Fig. 27c](#) are the optimized designs with the target number of tunnels $\tilde{T} = 1$ and $\tilde{T} = 2$, respectively. [Fig. 27b](#) and [Fig. 27d](#) are the whole optimized model of the first two cases, and the number of tunnels in these two designs is 16 and 20, respectively.

In the following two cases, the impact of different padding elements on SCC is investigated. As mentioned in Section 3.1, the topological numbers of an element are closely related to its 26-neighborhood $N_{26}(\tilde{v})$. Therefore, by padding different elements onto each edge, it is possible to alter the topological numbers of the elements on the edges of the design domain, thereby changing the topology of the structure. Instead of padding the whole design domain with void elements ([Fig. 27a](#) and [Fig. 27c](#)), the two inner edges of the design domain are padded with solid elements (see the white boundaries in [Fig. 27e](#) and [Fig. 27g](#)). Consequently, the topological features of these two cases are different from those of the first two cases ([Fig. 27a](#) and [Fig. 27c](#)). Although the same topological constraints are applied to the cases [Fig. 27e](#) ($\tilde{T} = 1$) and [Fig. 27g](#) ($\tilde{T} = 2$), respectively, the final results are quite

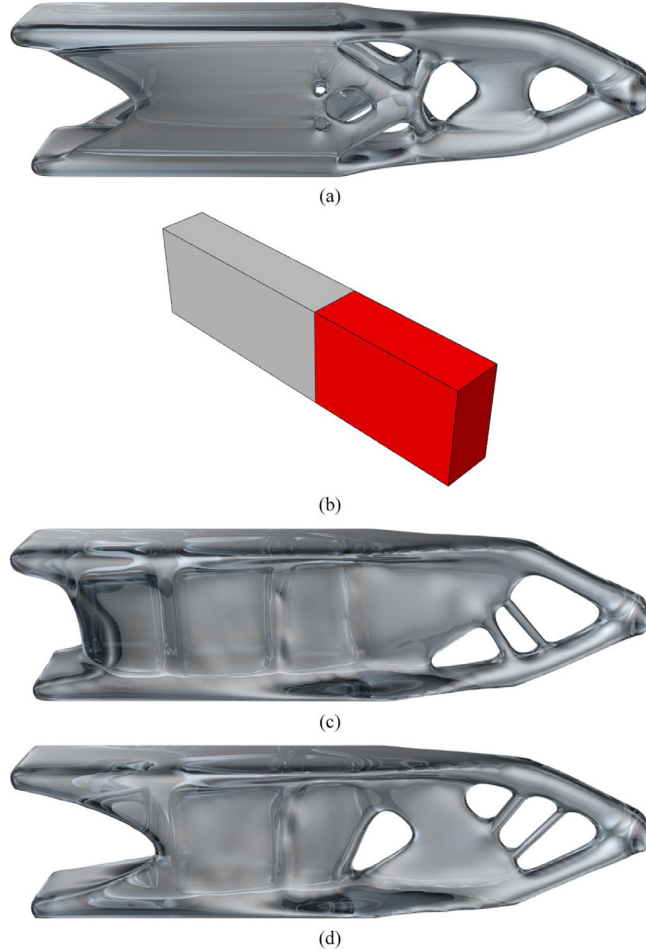


Fig. 25. Application of SCC in selected sub-regions. (a) Initial optimized design without SCC with a volume fraction of 35%. (b) Two selected regions. (c) Optimized design with $\tilde{C} = 3$ in white region and $\tilde{T} = 3$ in the red region. (d) Optimized design with $\tilde{C} = 2$ in white region and $\tilde{T} = 4$ in the red region. (For interpretation of the references to color in this figure legend, the reader is referred to the web version of this article.)

different. Since the inner two edges are padded with solid material, the number of concave shapes on the two edges will be identified as the number of newly generated tunnels (see the red arrow in Fig. 27g). Thus, the number of tunnels in Fig. 27e and Fig. 27g should be equal to the number of tunnels plus the number of concavities on the edges that are padded with solid elements. As shown in Fig. 27f and Fig. 27h, the number of tunnels in the two designs is 4 and 6, respectively. The results demonstrate that the padding strategy can efficiently regulate the removal of elements along structural edges.

Compared with the IO design (Fig. 26c), the structural compliances of the optimized structure in Fig. 27b, Fig. 27d, Fig. 27f and Fig. 27h are 4%, 2%, 19% and 15% lower, respectively. It demonstrates that designs with better performances can be generated by using the SCC approach to constrain the number of tunnels. A similar cantilever beam example was conducted by Villanueva and Maute [81]. It was found that the stiffest structure was closed-walled rather than frame-like. This matches the results of this study.

5. Extensions

This section shows the potential applications of the SCC approach in different areas, including avoiding enclosed cavities for additive manufacturing and creating diverse and competitive solutions for structural designs.

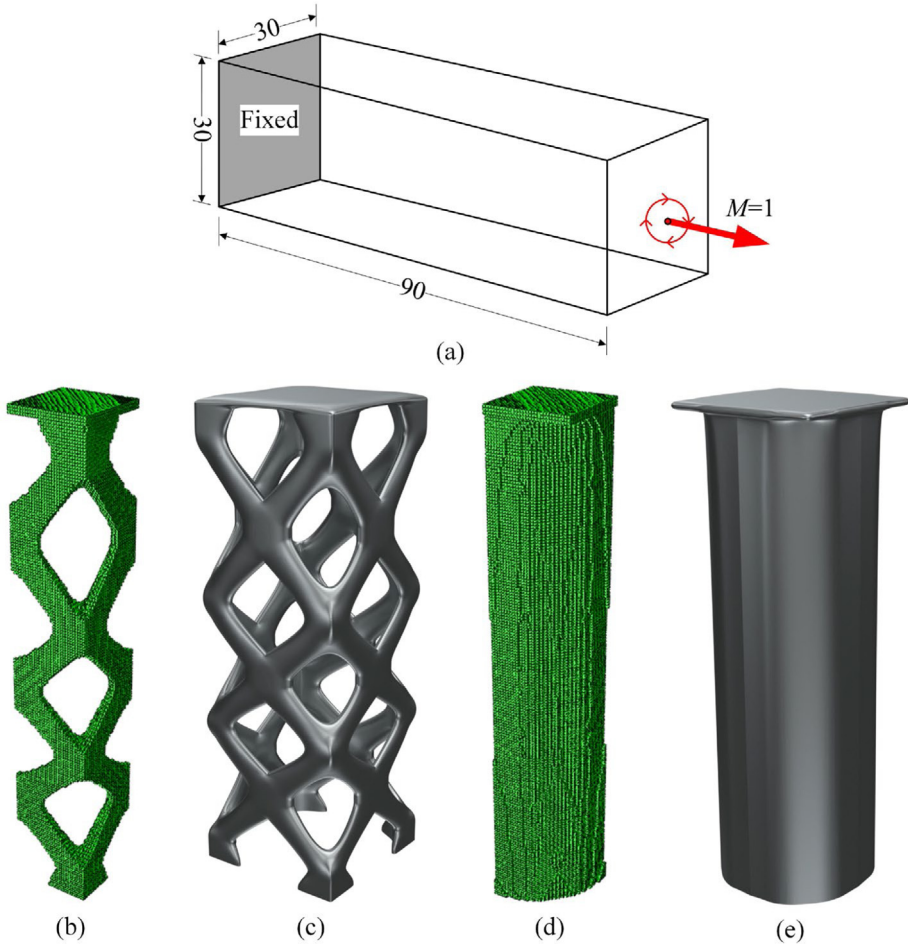


Fig. 26. Optimized designs of the three-dimensional cantilever beam without SCC. (a) Design domain and boundary conditions of the cantilever beam. (b) and (c) are the optimized designs without SCC, and the filter radius is 3. (d) and (e) are the optimized designs without SCC and filter scheme.

5.1. Avoiding enclosed cavities in a three-dimensional cantilever beam

In this example, a torsion cantilever beam is presented. Fig. 28a shows the loading and boundary conditions of the cantilever beam. The whole design domain is discretized by a $120 \times 40 \times 40$ element mesh. Three layers of elements on both two ends are prescribed as non-designable. The target volume fraction and the filter radius are 40% and 3, respectively. The minimum length scale constraint for Eq. (25) is $R_t = 1$. Due to symmetry, only a quarter of this model is optimized.

Fig. 28b shows the IO result without SCC. The sectional view in Fig. 28c shows a large cavity in the middle of the structure. To avoid enclosed cavities in the optimized designs, two cases with different target numbers of tunnels are presented in Figs. 29b and 29c ($\tilde{T} = 1$) and Figs. 29d and 29e ($\tilde{T} = 2$). The number of elements in each tunnel closure is required to be no smaller than 20. In the work reported by Xiong et al. [10], the enclosed cavity was eliminated by digging tunnels that connect the cavities with the structural boundary when the material volume

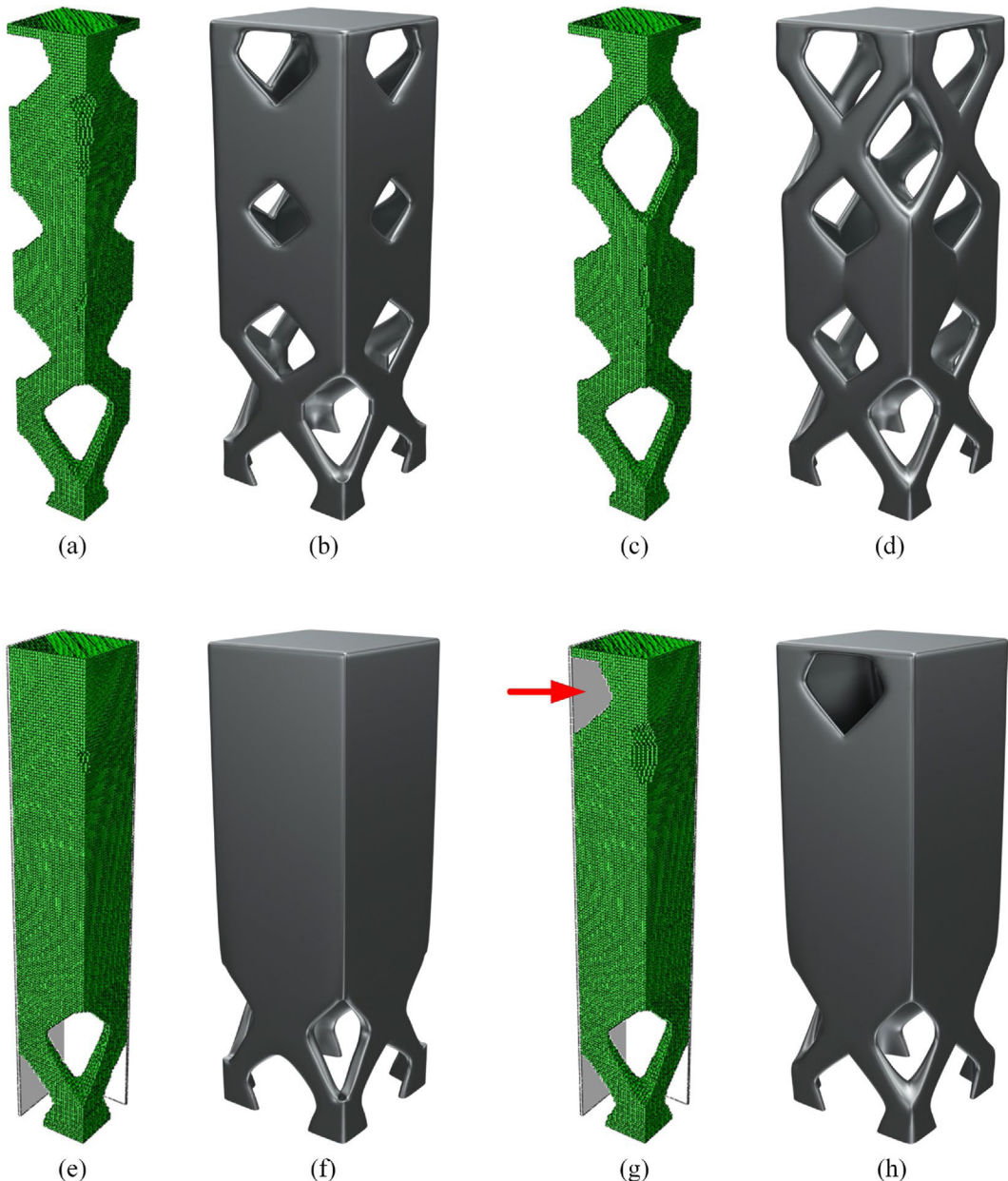


Fig. 27. Optimized designs of the three-dimensional cantilever beam with SCC. (a–b) Optimized design with $\tilde{T} = 1$. (b–d) Optimized design with $\tilde{T} = 2$. (e–f) Optimized design with $\tilde{T} = 1$. (g–h) Optimized design with $\tilde{T} = 2$. In (e–h), the two symmetrical planes are padded with solid elements. (For interpretation of the references to color in this figure legend, the reader is referred to the web version of this article.)

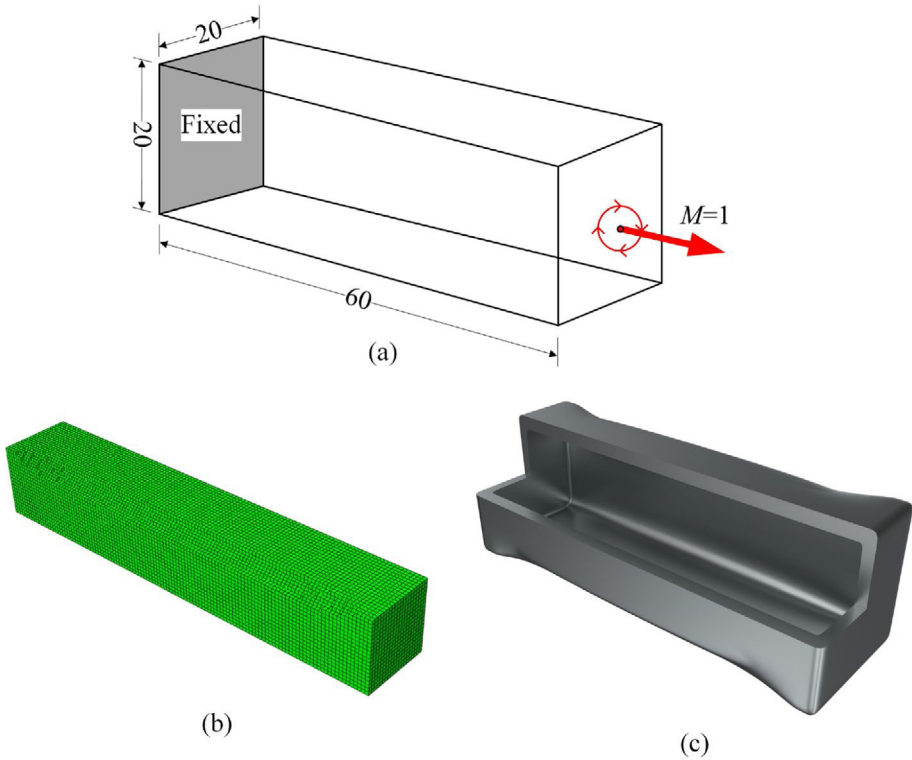


Fig. 28. The example of the three-dimensional cantilever beam. (a) Loading and boundary conditions of the cantilever beam. (b–c) The initial optimized design without SCC.

reached the final target value. In the present work, an initial design that contains a number of prescribed tunnels is specified (see Fig. 29a). Then, the SCC approach is used to optimize the structure by relocating the tunnels in the structure. The structural compliances of Fig. 29c and Fig. 29e are only 2% and 3% higher than that of the IO design (Fig. 28c), respectively. For the same example, the compliances increased by 3% and 6%, respectively in [10]. The results indicate that the proposed SCC approach can generate similar final designs with slightly lower structural compliances.

5.2. Diverse and competitive designs for a 3D arch bridge

In this example, a three-dimensional arch bridge is used to demonstrate the effectiveness of the SCC approach to achieve diverse design solutions by controlling the size of the tunnels [Eq. (24b)]. Fig. 30 shows the loading and boundary conditions of the three-dimensional arch bridge. A non-designable deck is in the middle of the design domain. Only a quarter of this model is considered for finite element analysis because of the symmetry. The size of each element is $0.5 \times 0.5 \times 0.5$. The target volume fraction is 8%, and the filter radius is 1.5. The minimum length scale constraint for Eq. (25) is $R_t = 0.5$.

Fig. 31a shows the IO design without SCC. In this design, two arches are located separately at each edge of the deck, creating a pathway for traffic in the middle of the deck.

In the next two cases (Fig. 31b and Fig. 31c), the SCC starts from the same initial design. In the first image of Fig. 32, the highlighted red region is the prescribed initial void domain. For each of the two cases, the prescribed initial topology is maintained during the whole optimization process by using the topology-preserving method [20]. As the original topology-preserving method cannot control the minimum size of the tunnels, this method can be

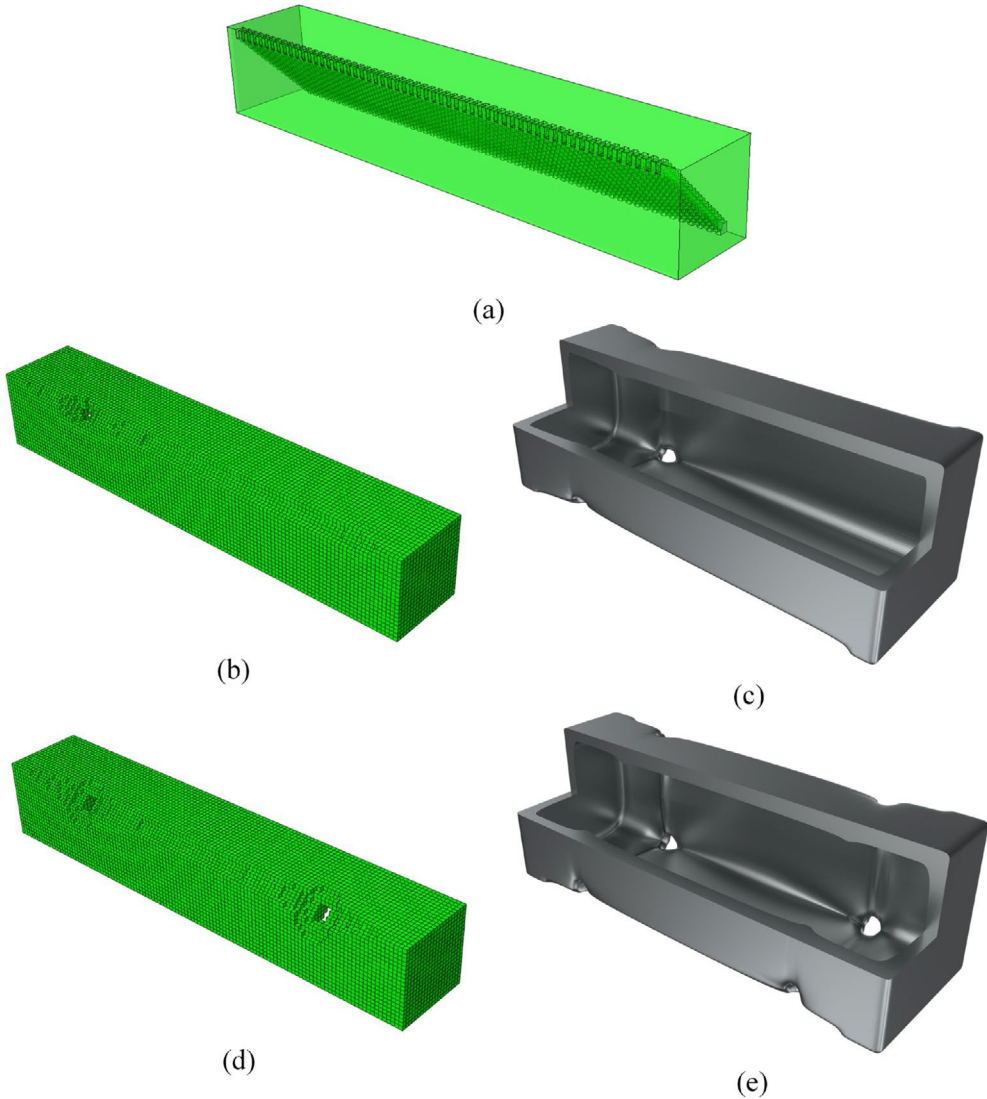


Fig. 29. Influence of initial design on optimized design. (a) Initial design with a prescribed number of tunnels. (b–c) Optimized design with $\tilde{T} = 1$. (d–e) Optimized design with $\tilde{T} = 2$.

extended by conducting shape optimization according to Eq. (24b) to control the minimum size of each tunnel. Fig. 31b and Fig. 31c show two different optimized designs. The number of elements in each tunnel closure is required to be greater than 30 for Fig. 31b and 60 for Fig. 31c. Compared with the IO design (Fig. 31a), the traffic flow in these two cases is routed into two lanes, as the pathway diverges at the bridge entrance. Moreover, the clearance between the road surface and overhead structures is directly controlled by the minimum size constraint of the tunnels. Fig. 32 presents the evolution history of case Fig. 31b. The compliance value of the two designs

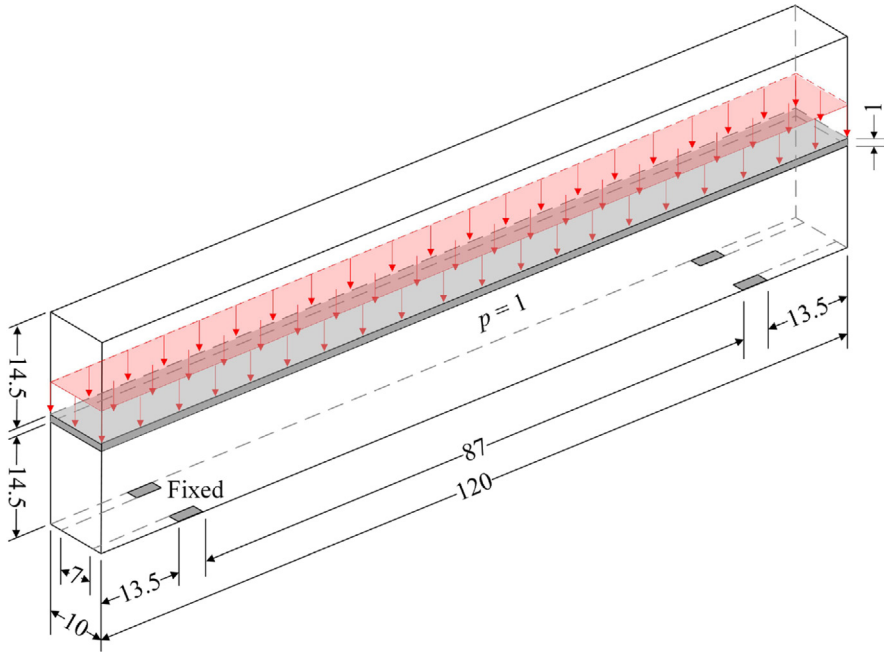


Fig. 30. Loading and boundary conditions of the three-dimensional arch bridge.

are 8% (Fig. 31b) and 14% (Fig. 31c) higher than that of the IO design (Fig. 31a). The results clearly demonstrate the effectiveness of the SCC approach in controlling the size of the tunnels. However, the designer has to select an acceptable performance penalty for achieving higher diversity from the SCC.

6. Conclusions

In this paper, we have developed a hole-filling method to directly control the structural complexity during the topology optimization process. Compared with most existing approaches, which can only control the number of cavities, the proposed approach is able to precisely constrain both the cavities and tunnels, thereby enabling the designer to participate in the structural form-finding process in a more direct manner. By using the developed structural complexity control (SCC) approach, the minimum length scale of the structure and the size of the cavities and tunnels can also be explicitly controlled. The effectiveness of the proposed approach is verified by several two- and three-dimensional compliance minimization problems. The capability of the SCC approach in creating diverse and competitive solutions is well demonstrated in the numerical examples. The developed approach has great potential to help engineers and architects search for efficient structural designs with controllable topologies.

Declaration of competing interest

The authors declare that they have no known competing financial interests or personal relationships that could have appeared to influence the work reported in this paper.

Data availability

Data will be made available on request.

Acknowledgments

This work is supported by the China Scholarship Council (201808430204), the Australian Research Council (FL190100014 and DE200100887) and the National Natural Science Foundation of China (12272034).

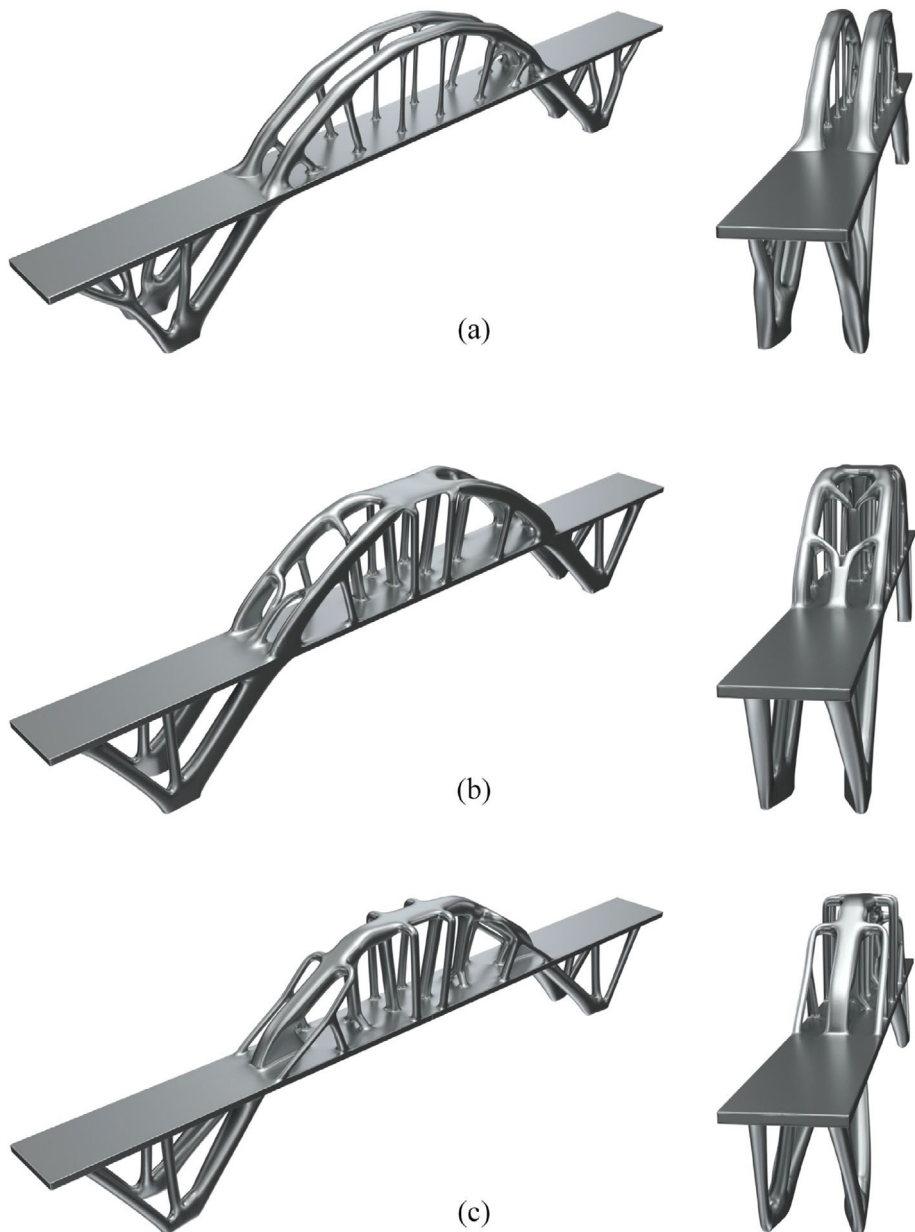


Fig. 31. (a) Optimized design without SCC. (b) Optimized design with SCC. In this case, the minimum size of each tunnel is greater than 30 elements. (c) Optimized design with SCC. In this case, the minimum size of each tunnel is greater than 60 elements.

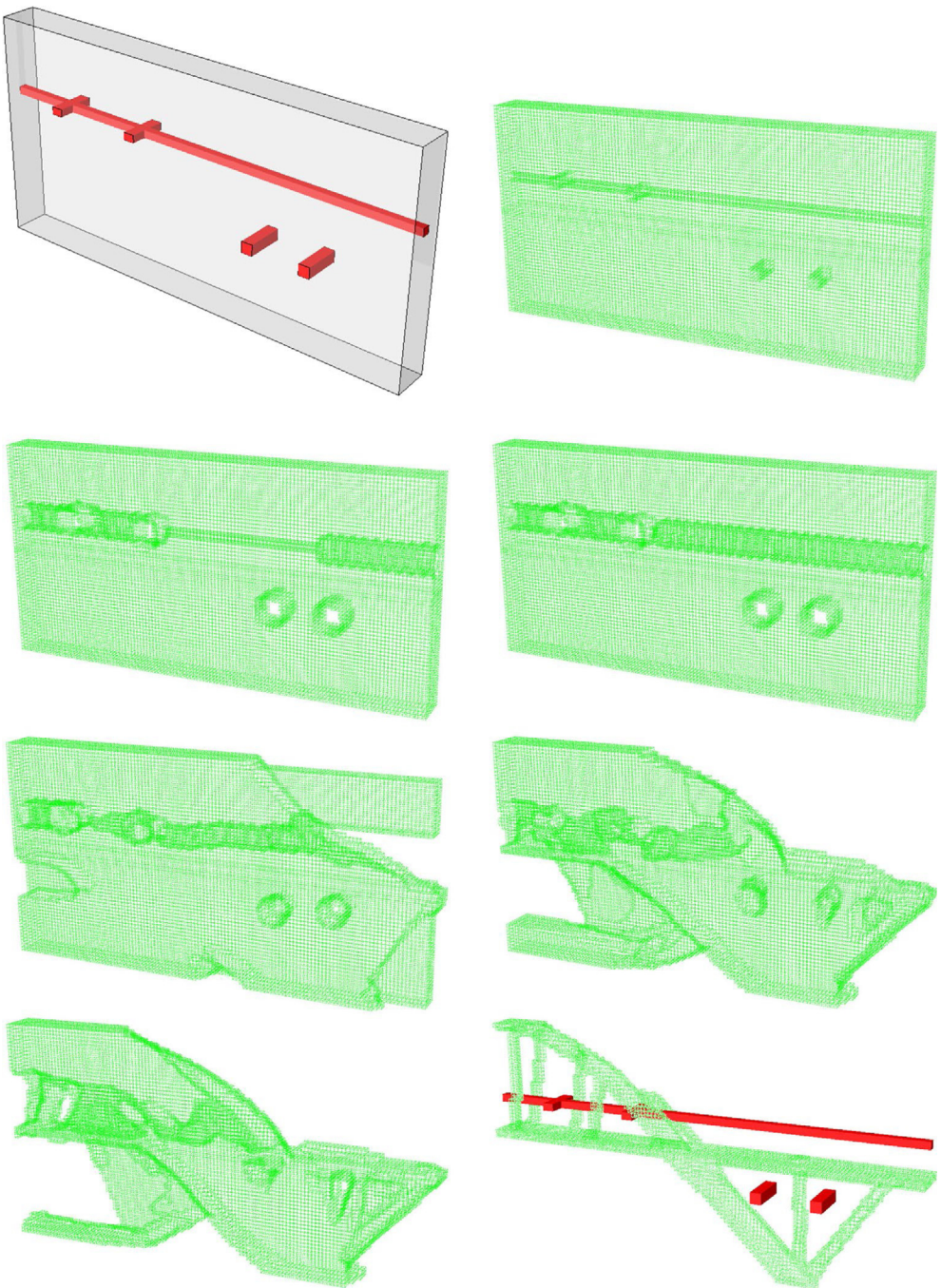


Fig. 32. Evolution history of case Fig. 31b. (For interpretation of the references to color in this figure legend, the reader is referred to the web version of this article.)

References

- [1] M.P. Bendsøe, N. Kikuchi, Generating optimal topologies in structural design using a homogenization method, *Comput. Methods Appl. Mech. Engrg.* 71 (1988) 197–224, [http://dx.doi.org/10.1016/0045-7825\(88\)90086-2](http://dx.doi.org/10.1016/0045-7825(88)90086-2).
- [2] M.P. Bendsøe, Optimal shape design as a material distribution problem, *Struct. Optim.* 1 (1989) 193–202, <http://dx.doi.org/10.1007/BF01650949>.
- [3] M.P. Bendsøe, O. Sigmund, *Topology Optimization: Theory, Methods, and Applications*, Springer, Berlin, 2004.
- [4] Y.M. Xie, G.P. Steven, A simple evolutionary procedure for structural optimization, *Comput. Struct.* 49 (1993) 885–896, [http://dx.doi.org/10.1016/0045-7949\(93\)90035-C](http://dx.doi.org/10.1016/0045-7949(93)90035-C).
- [5] Y.M. Xie, G.P. Steven, *Evolutionary Structural Optimization*, Springer, London, 1997.
- [6] X. Huang, Y.M. Xie, Convergent and mesh-independent solutions for the bi-directional evolutionary structural optimization method, *Finite Elem. Anal. Des.* 43 (2007) 1039–1049, <http://dx.doi.org/10.1016/j.finel.2007.06.006>.
- [7] X. Huang, Y.M. Xie, *Evolutionary Topology Optimization of Continuum Structures: Methods and Applications*, John Wiley & Sons, Chichester, UK, 2010.
- [8] M.Y. Wang, X. Wang, D. Guo, A level set method for structural topology optimization, *Comput. Methods Appl. Mech. Engrg.* 192 (2003) 227–246, [http://dx.doi.org/10.1016/S0045-7825\(02\)00559-5](http://dx.doi.org/10.1016/S0045-7825(02)00559-5).
- [9] G. Allaire, F. Jouve, A.M. Toader, Structural optimization using sensitivity analysis and a level-set method, *J. Comput. Phys.* 194 (2004) 363–393, <http://dx.doi.org/10.1016/j.jcp.2003.09.032>.
- [10] Y. Xiong, S. Yao, Z.L. Zhao, Y.M. Xie, A new approach to eliminating enclosed voids in topology optimization for additive manufacturing, *Addit. Manuf.* 32 (2020) 101006, <http://dx.doi.org/10.1016/j.addma.2019.101006>.
- [11] M. Bi, P. Tran, Y.M. Xie, Topology optimization of 3D continuum structures under geometric self-supporting constraint, *Addit. Manuf.* 36 (2020) 101422, <http://dx.doi.org/10.1016/j.addma.2020.101422>.
- [12] Y. Xiong, D. Bao, X. Yan, T. Xu, Y.M. Xie, Lessons learnt from a national competition on structural optimization and additive manufacturing, *Curr. Chin. Sci.* 1 (2021) 151–159, <http://dx.doi.org/10.2174/2666001601999201006191103>.
- [13] Z. Zhuang, Y.M. Xie, S. Zhou, A reaction diffusion-based level set method using body-fitted mesh for structural topology optimization, *Comput. Methods Appl. Mech. Engrg.* 381 (2021) 113829, <http://dx.doi.org/10.1016/j.cma.2021.113829>.
- [14] Z. Zhuang, Y.M. Xie, Q. Li, S. Zhou, Body-fitted bi-directional evolutionary structural optimization using nonlinear diffusion regularization, *Comput. Methods Appl. Mech. Engrg.* 396 (2022) 115114, <http://dx.doi.org/10.1016/j.cma.2022.115114>.
- [15] J. Ma, Z. Li, Z.L. Zhao, Y.M. Xie, Creating novel furniture through topology optimization and advanced manufacturing, *Rapid Prototyp. J.* (2021) <http://dx.doi.org/10.1108/RPJ-03-2021-0047>.
- [16] X. Yan, J. Chen, H. Hua, Y. Zhang, X. Huang, Smooth topological design of structures with minimum length scale and chamfer/round controls, *Comput. Methods Appl. Mech. Engrg.* 383 (2021) 113939, <http://dx.doi.org/10.1016/j.cma.2021.113939>.
- [17] Y.M. Xie, Generalized topology optimization for architectural design, *Archit. Intell.* 1 (2022) 2, <http://dx.doi.org/10.1007/s44223-022-00003-y>.
- [18] K. Yang, Z.L. Zhao, Y. He, S. Zhou, Q. Zhou, W. Huang, Y.M. Xie, Simple and effective strategies for achieving diverse and competitive structural designs, *Extreme Mech. Lett.* 30 (2019) 100481, <http://dx.doi.org/10.1016/j.eml.2019.100481>.
- [19] Y. He, K. Cai, Z.L. Zhao, Y.M. Xie, Stochastic approaches to generating diverse and competitive structural designs in topology optimization, *Finite Elem. Anal. Des.* 173 (2020) 103399, <http://dx.doi.org/10.1016/j.finel.2020.103399>.
- [20] Y. He, Z.L. Zhao, K. Cai, J. Kirby, Y. Xiong, Y.M. Xie, A thinning algorithm based approach to controlling structural complexity in topology optimization, *Finite Elem. Anal. Des.* 207 (2022) 103779, <http://dx.doi.org/10.1016/j.finel.2022.103779>.
- [21] Y. Rong, Z.L. Zhao, X.Q. Feng, Y.M. Xie, Structural topology optimization with an adaptive design domain, *Comput. Methods Appl. Mech. Engrg.* 389 (2022) 114382, <http://dx.doi.org/10.1016/j.cma.2021.114382>.
- [22] X. Yan, D. Bao, Y. Zhou, Y. Xie, T. Cui, Detail control strategies for topology optimization in architectural design and development, *Front. Archit. Res.* 11 (2022) 340–356, <http://dx.doi.org/10.1016/j foar.2021.11.001>.
- [23] X. Meng, Y. Xiong, Y.M. Xie, Y. Sun, Z.L. Zhao, Shape-thickness-topology coupled optimization of free-form shells, *Autom. Constr.* 142 (2022) 104476, <http://dx.doi.org/10.1016/j.autcon.2022.104476>.
- [24] Z. Li, T.U. Lee, Y.M. Xie, Interactive structural topology optimization with subjective scoring and drawing systems, *Comput. Aided Des.* 160 (2023) 103532, <http://dx.doi.org/10.1016/j.cad.2023.103532>.
- [25] Z.L. Zhao, S. Zhou, X.Q. Feng, Y.M. Xie, On the internal architecture of emergent plants, *J. Mech. Phys. Solids* 119 (2018) 224–239, <http://dx.doi.org/10.1016/j.jmps.2018.06.014>.
- [26] Z.L. Zhao, S. Zhou, X.Q. Feng, Y.M. Xie, Morphological optimization of scorpion telson, *J. Mech. Phys. Solids* 135 (2020) 103773, <http://dx.doi.org/10.1016/j.jmps.2019.103773>.
- [27] J. Ma, Z.L. Zhao, S. Lin, Y.M. Xie, Topology of leaf veins: Experimental observation and computational morphogenesis, *J. Mech. Behav. Biomed. Mater.* 123 (2021) 104788, <http://dx.doi.org/10.1016/j.jmbbm.2021.104788>.
- [28] S. Chu, Z. Yang, M. Xiao, H. Qiu, K. Gao, L. Gao, Explicit topology optimization of novel polyline-based core sandwich structures using surrogate-assisted evolutionary algorithm, *Comput. Methods Appl. Mech. Engrg.* 369 (2020) 113215, <http://dx.doi.org/10.1016/j.cma.2020.113215>.
- [29] Y. Rong, Z.L. Zhao, X.Q. Feng, J. Yang, Y.M. Xie, Computational morphomechanics of growing plant roots, *J. Mech. Phys. Solids* 178 (2023) 105346, <http://dx.doi.org/10.1016/j.jmps.2023.105346>.
- [30] A. Chen, K. Cai, Z.L. Zhao, Y. Zhou, L. Xia, Y.M. Xie, Controlling the maximum first principal stress in topology optimization, *Struct. Multidiscip. Optim.* 63 (2021) 327–339, <http://dx.doi.org/10.1007/s00158-020-02701-5>.
- [31] Y. Li, Y.M. Xie, Evolutionary topology optimization for structures made of multiple materials with different properties in tension and compression, *Compos. Struct.* 259 (2021) 113497, <http://dx.doi.org/10.1016/j.comstruct.2020.113497>.

- [32] T.U. Lee, Y.M. Xie, Simultaneously optimizing supports and topology in structural design, *Finite Elem. Anal. Des.* 197 (2021) 103633, <http://dx.doi.org/10.1016/j.finel.2021.103633>.
- [33] T.U. Lee, Y.M. Xie, Optimizing load locations and directions in structural design, *Finite Elem. Anal. Des.* 209 (2022) 103811, <http://dx.doi.org/10.1016/j.finel.2022.103811>.
- [34] K. Gao, D.M. Do, S. Chu, G. Wu, H.A. Kim, C.A. Featherston, Robust topology optimization of structures under uncertain propagation of imprecise stochastic-based uncertain field, *Thin-Walled Struct.* 175 (2022) 109238, <http://dx.doi.org/10.1016/j.tws.2022.109238>.
- [35] T. Xu, X. Lin, Y.M. Xie, Bi-directional evolutionary structural optimization with buckling constraints, *Struct. Multidiscip. Optim.* 66 (2023) 67, <http://dx.doi.org/10.1007/s00158-023-03517-9>.
- [36] H.W. Dong, S.D. Zhao, X.B. Miao, C. Shen, X. Zhang, Z. Zhao, C. Zhang, Y.S. Wang, L. Cheng, Customized broadband pentamode metamaterials by topology optimization, *J. Mech. Phys. Solids* 152 (2021) 104407, <http://dx.doi.org/10.1016/j.jmps.2021.104407>.
- [37] H.W. Dong, S.D. Zhao, Y.S. Wang, C. Zhang, Topology optimization of anisotropic broadband double-negative elastic metamaterials, *J. Mech. Phys. Solids* 105 (2017) 54–80, <http://dx.doi.org/10.1016/j.jmps.2017.04.009>.
- [38] W. Zhang, W. Zhong, X. Guo, Explicit layout control in optimal design of structural systems with multiple embedding components, *Comput. Methods Appl. Mech. Engrg.* 290 (2015) 290–313, <http://dx.doi.org/10.1016/j.cma.2015.03.007>.
- [39] M. Zhou, R. Fleury, Fail-safe topolobgy optimization, *Struct. Multidiscip. Optim.* 54 (2016) 1225–1243, <http://dx.doi.org/10.1007/s00158-016-1507-1>.
- [40] H. Wang, J. Liu, G. Wen, Y.M. Xie, The robust fail-safe topological designs based on the von Mises stress, *Finite Elem. Anal. Des.* 171 (2020) 103376, <http://dx.doi.org/10.1016/j.finel.2019.103376>.
- [41] J. Kirby, S. Zhou, Y.M. Xie, Optimal fail-safe truss structures: new solutions and uncommon characteristics, *Acta Mech. Sinica* 38 (2022) 421564, <http://dx.doi.org/10.1007/s10409-022-09028-3>.
- [42] A. Clausen, N. Aage, O. Sigmund, Topology optimization with flexible void area, *Struct. Multidiscip. Optim.* 50 (2014) 927–943, <http://dx.doi.org/10.1007/s00158-014-1109-8>.
- [43] S. Svensson, G.S.d. Baja, A tool for decomposing 3D discrete objects, in: *Proceedings of the 2001 IEEE Computer Society Conference on Computer Vision and Pattern Recognition, CVPR 2001*, 2001, p. I.
- [44] S. Svensson, C. Arcelli, G.S. di Baja, Characterising 3D objects by shape and topology, in: I. Nyström, G. Sanniti di Baja, S. Svensson (Eds.), *Discrete Geometry for Computer Imagery*, Springer Berlin Heidelberg, Berlin, Heidelberg, 2003, pp. 124–133.
- [45] S. Svensson, C. Arcelli, G.S.d. Baja, Finding cavities and tunnels in 3D complex objects, in: *12th International Conference on Image Analysis and Processing, 2003, Proceedings, 2003*, pp. 342–347.
- [46] C. Fiorio, J. Gustedt, Two linear time union-find strategies for image processing, *Theoret. Comput. Sci.* 154 (1996) 165–181, [http://dx.doi.org/10.1016/0304-3975\(94\)00262-2](http://dx.doi.org/10.1016/0304-3975(94)00262-2).
- [47] K. Wu, E. Otoo, A. Shoshani, *Optimizing Connected Component Labeling Algorithms*, SPIE, 2005.
- [48] W. Zhang, Y. Liu, P. Wei, Y. Zhu, X. Guo, Explicit control of structural complexity in topology optimization, *Comput. Methods Appl. Mech. Engrg.* 324 (2017) 149–169, <http://dx.doi.org/10.1016/j.cma.2017.05.026>.
- [49] Z.L. Zhao, S. Zhou, K. Cai, Y.M. Xie, A direct approach to controlling the topology in structural optimization, *Comput. Struct.* 227 (2020) 106141, <http://dx.doi.org/10.1016/j.compstruc.2019.106141>.
- [50] H. Han, Y. Guo, S. Chen, Z. Liu, Topological constraints in 2D structural topology optimization, *Struct. Multidiscip. Optim.* 63 (2021) 39–58, <http://dx.doi.org/10.1007/s00158-020-02771-5>.
- [51] Q. Wang, H. Han, C. Wang, Z. Liu, Topological control for 2D minimum compliance topology optimization using SIMP method, *Struct. Multidiscip. Optim.* 65 (2022) 38, <http://dx.doi.org/10.1007/s00158-021-03124-6>.
- [52] Y. Liang, X. Yan, G. Cheng, Explicit control of 2D and 3D structural complexity by discrete variable topology optimization method, *Comput. Methods Appl. Mech. Engrg.* 389 (2022) 114302, <http://dx.doi.org/10.1016/j.cma.2021.114302>.
- [53] B. Bourdin, Filters in topology optimization, *Internat. J. Numer. Methods Engrg.* 50 (2001) 2143–2158, <http://dx.doi.org/10.1002/nme.116>.
- [54] O. Sigmund, Morphology-based black and white filters for topology optimization, *Struct. Multidiscip. Optim.* 33 (2007) 401–424, <http://dx.doi.org/10.1007/s00158-006-0087-x>.
- [55] F. Wang, B.S. Lazarov, O. Sigmund, On projection methods, convergence and robust formulations in topology optimization, *Struct. Multidiscip. Optim.* 43 (2011) 767–784, <http://dx.doi.org/10.1007/s00158-010-0602-y>.
- [56] J.K. Guest, J.H. Prévost, T. Belytschko, Achieving minimum length scale in topology optimization using nodal design variables and projection functions, *Internat. J. Numer. Methods Engrg.* 61 (2004) 238–254, <http://dx.doi.org/10.1002/nme.1064>.
- [57] J.K. Guest, Imposing maximum length scale in topology optimization, *Struct. Multidiscip. Optim.* 37 (2009) 463–473, <http://dx.doi.org/10.1007/s00158-008-0250-7>.
- [58] X. Guo, W. Zhang, W. Zhong, Explicit feature control in structural topology optimization via level set method, *Comput. Methods Appl. Mech. Engrg.* 272 (2014) 354–378, <http://dx.doi.org/10.1016/j.cma.2014.01.010>.
- [59] W. Zhang, W. Zhong, X. Guo, An explicit length scale control approach in SIMP-based topology optimization, *Comput. Methods Appl. Mech. Engrg.* 282 (2014) 71–86, <http://dx.doi.org/10.1016/j.cma.2014.08.027>.
- [60] Q. Xia, T. Shi, Constraints of distance from boundary to skeleton: for the control of length scale in level set based structural topology optimization, *Comput. Methods Appl. Mech. Engrg.* 295 (2015) 525–542, <http://dx.doi.org/10.1016/j.cma.2015.07.015>.
- [61] H. Kim, O.M. Querin, G.P. Steven, Y.M. Xie, A method for varying the number of cavities in an optimized topology using Evolutionary Structural Optimization, *Struct. Multidiscip. Optim.* 19 (2000) 140–147, <http://dx.doi.org/10.1007/s001580050094>.
- [62] W. Zhang, J. Zhou, Y. Zhu, X. Guo, Structural complexity control in topology optimization via moving morphable component (MMC) approach, *Struct. Multidiscip. Optim.* 56 (2017) 535–552, <http://dx.doi.org/10.1007/s00158-017-1736-y>.
- [63] O. Sigmund, N. Aage, E. Andreassen, On the (non-)optimality of Michell structures, *Struct. Multidiscip. Optim.* 54 (2016) 361–373, <http://dx.doi.org/10.1007/s00158-016-1420-7>.

- [64] S. Liu, Q. Li, W. Chen, L. Tong, G. Cheng, An identification method for enclosed voids restriction in manufacturability design for additive manufacturing structures, *Front. Mech. Eng.* 10 (2015) 126–137, <http://dx.doi.org/10.1007/s11465-015-0340-3>.
- [65] L. Zhou, W. Zhang, Topology optimization method with elimination of enclosed voids, *Struct. Multidiscip. Optim.* 60 (2019) 117–136, <http://dx.doi.org/10.1007/s00158-019-02204-y>.
- [66] J.P. Kruth, P. Mercelis, J. Van Vaerenbergh, L. Froyen, M. Rombouts, Binding mechanisms in selective laser sintering and selective laser melting, *Rapid Prototyp. J.* 11 (2005) 26–36, <http://dx.doi.org/10.1108/13552540510573365>.
- [67] I. Zein, D.W. Hutmacher, K.C. Tan, S.H. Teoh, Fused deposition modeling of novel scaffold architectures for tissue engineering applications, *Biomaterials* 23 (2002) 1169–1185, [http://dx.doi.org/10.1016/S0142-9612\(01\)00232-0](http://dx.doi.org/10.1016/S0142-9612(01)00232-0).
- [68] H. Han, C. Wang, T. Zuo, Z. Liu, Inequality constraint on the maximum genus for 3D structural compliance topology optimization, *Sci. Rep.* 12 (2022) 16185, <http://dx.doi.org/10.1038/s41598-022-20248-x>.
- [69] Z. Aktouf, G. Bertrand, L. Perrotin, A three-dimensional holes closing algorithm, *Pattern Recognit. Lett.* 23 (2002) 523–531.
- [70] Z. Aktouf, G. Bertrand, L. Perrotin, A 3D-hole closing algorithm, in: S. Miguet, A. Montanvert, S. Ubéda (Eds.), *Discrete Geometry for Computer Imagery*, Springer Berlin Heidelberg, Berlin, Heidelberg, 1996, pp. 36–47.
- [71] L. Xia, Q. Xia, X. Huang, Y.M. Xie, Bi-directional evolutionary structural optimization on advanced structures and materials: a comprehensive review, *Arch. Comput. Methods Eng.* 25 (2018) 437–478, <http://dx.doi.org/10.1007/s11831-016-9203-2>.
- [72] O. Sigmund, J. Petersson, Numerical instabilities in topology optimization: a survey on procedures dealing with checkerboards, mesh-dependencies and local minima, *Struct. Optim.* 16 (1998) 68–75, <http://dx.doi.org/10.1007/BF01214002>.
- [73] Z.H. Zuo, Y.M. Xie, A simple and compact Python code for complex 3D topology optimization, *Adv. Eng. Softw.* 85 (2015) 1–11, <http://dx.doi.org/10.1016/j.advengsoft.2015.02.006>.
- [74] T.Y. Kong, A. Rosenfeld, Digital topology: Introduction and survey, *Comput. Vis. Graph. Image Process.* 48 (1989) 357–393, [http://dx.doi.org/10.1016/0734-189X\(89\)90127-8](http://dx.doi.org/10.1016/0734-189X(89)90127-8).
- [75] G. Bertrand, Simple points, topological numbers and geodesic neighborhoods in cubic grids, *Pattern Recognit. Lett.* 15 (1994) 1003–1011, [http://dx.doi.org/10.1016/0167-8655\(94\)90032-9](http://dx.doi.org/10.1016/0167-8655(94)90032-9).
- [76] G. Malandain, G. Bertrand, N. Ayache, Topological segmentation of discrete surfaces, *Int. J. Comput. Vis.* 10 (1993) 183–197, <http://dx.doi.org/10.1007/BF01420736>.
- [77] T.C. Lee, R.L. Kashyap, C.N. Chu, Building skeleton models via 3-D medial surface axis thinning algorithms, *CVGIP, Graph. Models Image Process.* 56 (1994) 462–478, <http://dx.doi.org/10.1006/cgip.1994.1042>.
- [78] Y.F. Tsao, K.S. Fu, A 3D parallel skeletonwize thinning algorithm, in: *IEEE Conference on Pattern Recognition and Image Processing*, 1982, pp. 678–683.
- [79] G. Borgefors, Distance transformations in digital images, *Comput. Vis. Graph. Image Process.* 34 (1986) 344–371, [http://dx.doi.org/10.1016/S0734-189X\(86\)80047-0](http://dx.doi.org/10.1016/S0734-189X(86)80047-0).
- [80] P. Soille, *Morphological Image Analysis: Principles and Applications*, Springer, 1999.
- [81] C.H. Villanueva, K. Maute, Density and level set-XFEM schemes for topology optimization of 3-D structures, *Comput. Mech.* 54 (2014) 133–150, <http://dx.doi.org/10.1007/s00466-014-1027-z>.